Locating star-forming regions in quasar host galaxies[*]

J. E. Young,[1,2]† M. Eracleous,[1,2,3] O. Shemmer,[4] H. Netzer,[5] C. Gronwall,[1,2] Dieter Lutz,[6] R. Ciardullo[1,2] and Eckhard Sturm[6]

[1]*Department of Astronomy and Astrophysics, The Pennsylvania State University, 525 Davey Lab, University Park, PA 16802, USA*
[2]*Institute for Gravitation and the Cosmos, The Pennsylvania State University, University Park, PA 16802, USA*
[3]*Kavli Institute for Theoretical Physics, The University of California, Santa Barabara, CA 93106, USA*
[4]*Department of Physics, University of North Texas, Denton, TX 76203, USA*
[5]*School of Physics and Astronomy and the Wise Observatory, Raymond and Beverly Sackler Faculty of Exact Sciences, Tel Aviv University, Tel Aviv 03-7441142, Israel*
[6]*Max-Planck-Institut fur Extraterrestrische Physik, D-85741 Garching bei München, Germany*

ABSTRACT

We present a study of the morphology and intensity of star formation in the host galaxies of eight Palomar-Green quasars using observations with the *Hubble Space Telescope*. Our observations are motivated by recent evidence for a close relationship between black hole growth and the stellar mass evolution in its host galaxy. We use narrow-band [O II]λ3727, Hβ, [O III]λ5007 and Paα images, taken with the Wide Field Planetary Camera 2 and NICMOS instruments, to map the morphology of line-emitting regions, and, after extinction corrections, diagnose the excitation mechanism and infer star-formation rates. Significant challenges in this type of work are the separation of the quasar light from the stellar continuum and the quasar-excited gas from the star-forming regions. To this end, we present a novel technique for image decomposition and subtraction of quasar light. Our primary result is the detection of extended line-emitting regions with sizes ranging from 0.5 to 5 kpc and distributed symmetrically around the nucleus, powered primarily by star formation. We determine star-formation rates of the order of a few tens of M$_\odot$ yr^{-1}. The host galaxies of our target quasars have stellar masses of the order of 10^{11} M$_\odot$ and specific star-formation rates on a par with those of M82 and luminous infrared galaxies. As such they fall at the upper envelope or just above the star-formation mass sequence in the specific star formation versus stellar mass diagram. We see a clear trend of increasing star-formation rate with quasar luminosity, reinforcing the link between the growth of the stellar mass of the host and the black hole mass found by other authors.

Key words: ISM: lines and bands – quasars: general – galaxies: starburst.

1 INTRODUCTION

Over the past decade a number of observational results have pointed to a link between the growth of galactic bulges and that of the supermassive black holes in galactic centres. Relationships were first found between central black hole mass (M_{BH}) and the host spheroid luminosity (L_{bulge}, e.g. Kormendy & Richstone 1995; McLure & Dunlop 2001; Marconi & Hunt 2003). Later, the relationship between the black hole mass and the stellar velocity dispersion ($\sigma_\star$), the so-called $M_{BH}-\sigma_\star$ relation, was found in both active and inactive galaxies (e.g. Ferrarese & Merritt 2000; Gebhardt et al. 2000;

Nelson 2000; Ferrarese et al. 2001; Tremaine et al. 2002; Onken et al. 2003). These observations strongly suggest a physical mechanism linking the growth of the central black hole with the growth of the spheroid.

It is now thought that much of the growth of the central black hole and the formation of the galactic bulge are fuelled by the dissipative collapse of cool gas, often triggered by the merger of two galaxies. Ultraluminous Infrared Galaxies (ULIRGs) were suggested by Kormendy & Sanders (1992) to be the sites of intense star formation resulting from major mergers. This hypothesis was grounded by the fact that the red stellar populations of elliptical galaxies are best explained by a single, massive star-forming event of this magnitude. Ground-based optical imaging later confirmed that many ULIRGs are disturbed or interacting, and millimetre observations have shown them to be gas rich (Sanders 2001), bolstering this hypothesis. An additional confirmation comes from Netzer et al. (2007), who report that the far-infrared (FIR) excess in ULIRGs is due to vigorous star-forming activity.

A connection between quasars and ULIRGs was suggested by Sanders (2001) and later confirmed by Veilleux et al. (2006), who identified several Palomar-Green Quasars as ULIRGs and pointed out that the two populations are statistically indistinguishable. In this paradigm, ULIRGs are viewed as precursors to quasars, before much of the galaxy's gas is driven out and the star formation has been partly quenched. High-resolution optical imaging of quasar hosts (Disney et al. 1995; Bahcall et al. 1997; Guyon, Sanders & Stockton 2006; Veilleux et al. 2009; Cales et al. 2011) supports this line of reasoning by establishing that many quasar hosts show signs of interaction or disturbance. At the same time, *Herschel* observations of outflows in ULIRGs (Sturm et al. 2011) indicate that ULIRGs are capable of driving out their gas supply in 10^6–10^8 yr, again suggesting that ULIRGs and quasars fit into the same family of objects.

Nevertheless, the paradigm of quasars quenching their own growth and the star formation in their host galaxies remains uncertain. Rosario et al. (2013) use *Chandra*, *Hubble Space Telescope* (*HST*) and *Herschel* observations to show that UV-to-optical colours of galaxies with active galactic nuclei (hereafter AGNs) match those of equally massive inactive galaxies. They conclude that AGNs are more likely to be found in normal massive star-forming galaxies than in quenched galaxies transitioning from the blue to red sequences. Likewise, Mullaney et al. (2012) report no correlation between *Herschel* FIR and *Chandra* X-ray luminosities of low-level AGN host galaxies, indicating that global star formation is decoupled from nuclear activity for this class of objects. Supporting this conjecture, Santini et al. (2012) use *Chandra* and *Herschel* observations to show that nuclear activity in low-level AGN is decoupled from star formation while indicating that nuclear activity in high-luminosity AGN is contemporaneous with star formation.

The issue is further complicated by works, such as Cisternas et al. (2011), which report that low-redshift quasars hosts are no more likely to show signs of interaction than inactive galaxies, suggesting that internal secular processes and minor mergers are primarily responsible for black hole accretion and the attendant buildup of stellar populations. Likewise, Tacconi et al. (2002) find evidence from stellar dynamics that ULIRGs are unlikely to evolve into quasars, and Dasyra et al. (2007) report that Palomar–Green (PG) quasars may have a different formation mechanism than quasars with black holes more massive than 5×10^8 M$_\odot$. Furthermore, Ho (2005) finds the [O II]λ3727 doublet, another star-formation indicator, to be very weak or absent in long-slit spectra of PG quasars and suggests that star formation may be suppressed, calling into question the notion that quasar hosts are the sites of star formation. The view that quasars suppress star formation in their host galaxies is supported by Page et al. (2012) who find that star-formation activity declines with increasing X-ray luminosity among AGN at $z = 1$–3.

Indications of intense star-forming activity in the host galaxies of quasars, albeit at lower levels than those seen in ULIRGs, support the hypothesis that central black hole growth and stellar spheroid formation are causally connected. For instance, mid-infrared spectra taken with the *Spitzer* Space Telescope reveal 7.7 μm polycyclic aromatic hydrocarbon (PAH) emission in quasars at $z \sim 0.1$ (Schweitzer et al. 2006) and $z \sim 2$ (Lutz et al. 2008), which several authors (e.g. Förster Schreiber et al. 2004; Calzetti et al. 2007) link with star-forming activity. In the same spirit, Rigopoulou et al. (2009) find evidence of vigorous star formation in the host galaxies of type 2 quasars based on their FIR/sub-mm spectral energy distributions (SEDs). The connection between nuclear activity and star-formation is underscored by the presence of extremely active star-forming complexes in the host galaxies of AGNs. UV images

(e.g. Heckman et al. 1995, 1997; Colina et al. 1997) and spectra (e.g. Cid Fernandes, Storchi-Bergmann & Schmitt 1998; González Delgado, Heckman & Leitherer 2001) of Seyfert galaxies reveal young stellar populations, suggesting that star-forming complexes are characteristic of galaxies whose central black holes are accreting at high rates. There are also several less direct lines of evidence linking quasars to star formation. For example, a number of authors (e.g. Hamann & Ferland 1999, and references therein) identify super-solar metallicity in the broad line regions of quasars, while Shemmer et al. (2004) report a correlation between metallicity and the Eddington ratio over three orders of magnitude in luminosity. Finally, Cales et al. (2011) focus on post-starburst quasars, finding evidence that many are evolving towards E+A galaxies with morphological evidence to suggest that the outbursts are triggered by interactions or disturbances.

At the same time, other works address the physical mechanism for the correlation between star formation and black hole growth. Disturbed and interacting galaxies typically show enhanced star-forming activity (e.g. Schombert, Wallin & Struck-Marcell 1990; Hibbard & van Gorkom 1996), suggesting that tidal torques drive gas to the centres of galaxies, fuelling both stellar spheroid and black hole growth. Approaching the problem from a different direction, Kauffmann & Haehnelt (2000) use semi-analytic models to suggest a link between galactic mergers and black hole growth. They follow the mergers of dark matter haloes and assume that central black holes consume a few per cent of their host's gas during each merger. Their work is able to reproduce the observed $M_{BH}-L_{bulge}$ relationship as well as evolution in the quasar luminosity function over redshift. Volonteri, Haardt & Madau (2003a) and Volonteri, Madau & Haardt (2003b) follow the growth and merging of supermassive black holes through galactic merger trees from primordial seed black holes all the way to the central black holes of large elliptical galaxies. They strengthen the argument by finding that, in their simulation, most of a central black hole's mass results from accretion during mergers rather than the merger of two central black holes. Simulation-based studies that consider galaxy mergers and subsequent star formation and black hole accretion (e.g. Di Matteo, Springel & Hernquist 2005; Springel, Di Matteo & Hernquist 2005; Hopkins et al. 2005, 2006; Cox et al. 2008; Debuhr, Quataert & Ma 2011) can reproduce the observed $M_{BH}-\sigma_\star$ relationship. Moreover, such simulations explain the quasar luminosity versus stellar population correlations mentioned above, and cleanly recreate the transition from late-type to early-type galaxies. However, given the many and varied assumptions involved in these simulations, further guidance from observations is needed.

Yet another complexity arises in Bennert et al. (2002), who find a correlation between quasar luminosities and the sizes of AGN narrow-line regions. However, Netzer et al. (2004) point out that the AGN narrow-line region size relationship described by Bennert et al. (2002) would predict extremely large AGN narrow-line regions (exceeding 70 kpc for some quasars), AGN narrow-line region gas masses (up to 10^{10} M$_\odot$), and gas ejection rates (approaching $10^6 R_{10}$ M$_\odot$ yr^{-1}, where R_{10} is radial distance in units of 10 kpc). The existence of such large gas masses in the vicinity of quasars would have significant ramifications for the link between black hole and galaxy growth; but Netzer et al. (2004) argue this scenario is not compatible with AGN theory, and any correlation between luminosity and AGN narrow-line region size must break down at the luminosities of quasars.

Because of their importance, the theoretical scenarios for galaxy and quasar co-evolution have been subjected to a variety of observational tests. Boyce et al. (1996) study three *IRAS* selected quasar

hosts in the optical and find all three to be violently interacting, but later Boyce et al. (1998) find that only those three out of a larger sample of 14 quasar hosts, selected to have a broader range of properties, are engaged in violent interactions. Meanwhile, Gabor et al. (2009) use *HST* Advanced Camera for Surveys (ACS) images and Cosmic Evolution Survey (COSMOS) spectroscopy to demonstrate that AGN hosts are no more likely to be suffering strong interactions than normal galaxies. Conversely, Guyon et al. (2006) use near-IR adaptive optics to survey 32 PG quasars and find that 30 per cent show obvious signs of disturbance. This fraction is high enough to suggest a relationship between quasar ignition and galaxy interaction, but they also point out that either signs of disturbed morphology fade sooner than black hole accretion and star formation are quenched, or that not all quasars are triggered by external disturbances. The latter possibility is supported by Weinzirl et al. (2009) and Genzel et al. (2008), who find that secular processes are capable of driving gas in discs towards the galactic centres. Complicating the physical picture further, Hopkins (2009) and Governato et al. (2009) demonstrate that galaxies may reform discs in the wake of even violent mergers, casting doubt on the simple model of ellipticals as the ubiquitous end products of mergers.

One approach to these open questions is to image quasar host galaxies and use multiple narrow-band images to unambiguously map out star-forming regions while simultaneously surveying the objects signs of morphological disturbances resulting from mergers. The large contrast between the luminosity of a high accretion rate quasar and a typical host galaxy makes detailed observations of these most interesting and most active examples of this class difficult. The problem is exacerbated by the proximity of star-forming complexes to the central black hole in typical AGN hosts. For example, the UV luminous star-forming knots and rings found in nearby Seyfert galaxies by Colina et al. (1997) were within 1–2 kpc of the nuclei of their respective hosts. Bennert et al. (2002) find the AGN narrow-line regions of six of seven quasar hosts in Hβ images have galactocentric radii less than 6 kpc. Thus, adaptive optics or imaging from space is needed to resolve quasar hosts. In this work, we employ the latter method, using the Wide Field Planetary Camera 2 (WFPC2) and Near Infrared Camera and Multi-Object Spectrometer (NICMOS) instruments on the *HST* to observe eight nearby ($z \sim 0.1$) quasar host galaxies and to map star-forming regions and make measurements of star-formation rates (hereafter SFRs). The feasibility of this approach has been demonstrated by earlier works; for example, using broad-band WFPC2 images Bahcall et al. (1997) detect host galaxies around all 20 quasars in their sample, and McLeod & McLeod (2001) use NICMOS to detect host galaxies of 16 quasars in the near-IR.

As discussed above, narrow-band filters centred around emission lines, such as [O III]λ5007, profit from better galaxy to quasar contrast; this benefit is seen in Bennert et al. (2002), where the AGN narrow-line regions of seven quasars are observed with WFPC2 in ramp filters centred on [O III]λ5007. We expand upon this strategy by observing our quasars in [O III]λ5007, [O II]λ3727, Hβ, and Paα in ramp and narrow-band filters. This combination of emission lines also enables us to address the question of suppressed star formation discussed in Ho (2005) by distinguishing star-forming regions from AGN narrow-line regions through the use of line diagnostic diagrams.

In Section 2, we describe our observations and observing strategy. In Section 3, we outline the data reduction steps, including the use of the software package MULTIDRIZZLE to combine sub-exposures. In Section 4, we detail our novel point spread function (PSF) subtraction technique, which we verify in Section 5 through an analysis of simulated quasar+galaxy images to confirm the reliability of this method. In Section 6, we analyse the PSF-subtracted quasar host galaxies, including removal of stellar continuum an extinction correction. In Section 7, we discuss the contributions of different sources of measurement error to our final uncertainties. Finally, in Section 8 we report on the content and analysis of the processed host galaxy images, and in Section 9 we discuss the implications of these findings. For this work, we assume $H_0 = 69.32\ \mathrm{km\ s^{-1}\ Mpc^{-1}}$ with $\Omega_\mathrm{M} = 0.27$ and $\Omega_\Lambda = 0.73$.

2 SAMPLE SELECTION AND OBSERVING STRATEGY

We drew our targets from the *Spitzer* Infrared Spectrograph (IRS) sample of Schweitzer et al. (2006), selecting objects with redshifts such that the Paα line fell within one of the narrow-band NICMOS filters. Among the objects that meet these criteria, the eight nearest ($z < 0.15$) and brightest ($V < 16.5$) quasars are the targets for this project. These are listed in Table 1 along with their basic properties. The PAH luminosities of our targets span a range of two orders of magnitude.

Our work focuses on narrow-band images centred on the Paα, Hβ, and [O III]λ5007, and [O II]λ3727 lines. By selection, the Paα lines of our targets fell within one of the NICMOS narrow-band filters, listed in Table 2. To observe our targets in the optical bands, we used the WFPC2 camera. Typical exposure times in the emission-line filters were of the order of several thousand seconds. By using the ramp filters, we were able to select narrow-bands centred at the observed wavelengths of the desired emission lines. The ramp filters chosen are also listed in Table 2. Since the wavelength range of a ramp filter is set by the position of the object on the detector, most of our observations had to be made with one of the WF detectors rather than the PC detector. In several cases, one of the emission lines serendipitously fell within the *FQUVN* redshifted [O II] quadrant filter (central wavelength depends on quadrant but ranges from 3763 Å to 3992 Å); this filter was used in these cases. In two cases our quasar had previously been observed for a similar project (Bennert et al. 2002). For these objects, PG 0026+129 and PG 1307+085, we used archival [O III]λ5007 images. The observation dates for all the images of our eight quasars are listed in Table 3.

Observing both the Paα and Hβ lines allows us to correct for reddening. Also, with the use of the line-ratio diagnostic methods first described in Baldwin, Phillips, & Terlevich (1981) and developed further by other authors in later papers (e.g. Kewley et al. 2001; Groves, Dopita & Sutherland 2004a,b; Dopita et al. 2006, see Section 8.2), the relative intensities of the [O III]λ5007, [O II]λ3727 and Hβ lines allow us to distinguish between line emission produced by star-forming activity and line emission stimulated by the ionizing radiation of the quasars themselves, as well as composite systems where both star formation and quasar photoionization contribute to the line emission. Although the diagnostic line ratios involving Hα are often used in spectroscopic studies (e.g. Veilleux & Osterbrock 1987; Kewley et al. 2006), this was not possible in our narrow-band imaging study because the available filters could not separate the Hα and [N II]λλ6548, 6583 lines. Finally, after star-forming regions are identified, their Paα and Hβ luminosities give us two fairly direct measures of SFRs.

Additionally, we observed the quasars in medium-band filters, giving us continuum images of the host galaxies. To obtain the infrared continuum images, we observed each quasar in a medium-band filter centred on a wavelength near the Paα line. Specifically, we used the NICMOS2 *F237M* and NICMOS3 *F222M* filters. Due

Table 1. Target quasars and their basic properties.

Quasar	z	$m_V{}^a$ (mag)	$M_V{}^a$ (mag)	$L_{\mathrm{PAH\,7.7\mu m}}{}^b$ (erg s^{-1})	$L_{\mathrm{[Ne\,II]\,12.8\mu m}}{}^b$ (erg s^{-1})	$L_{\mathrm{FIR}}{}^c$ (erg s^{-1})	$\log(M_{\mathrm{BH}}/M_\odot)$	$D_L{}^f$ (Mpc)	$S_P{}^g$ $\left(\frac{\mathrm{kpc}}{\mathrm{pix}}\right)$
PG 0026+129	0.1420	14.8	−24.2	$<4.28 \times 10^{42}$	1.13×10^{41}	$<5.1 \times 10^{44}$	7.42 ± 0.07^d	681	0.13
PG 0838+770	0.1310	15.7	−23.1	4.38×10^{42}	1.73×10^{41}	8.4×10^{44}	8.2 ± 0.08^e	623	0.12
PG 1244+026	0.0482	16.2	−20.4	3.18×10^{41}	4.97×10^{40}	2.5×10^{44}	6.5 ± 0.08^e	216	0.05
PG 1307+085	0.1550	15.3	−23.8	$<1.28 \times 10^{42}$	2.45×10^{41}	9.7×10^{44}	8.51 ± 0.1^d	749	0.14
PG 1448+273	0.0650	15.0	−22.2	1.49×10^{42}	4.86×10^{40}	–	7.0 ± 0.08^e	295	0.06
PG 1613+658	0.1290	15.5	−23.3	1.56×10^{43}	1.57×10^{40}	2.5×10^{45}	7.37 ± 0.2^d	613	0.12
PG 1626+554	0.1330	16.2	−22.6	3.08×10^{42}	3.00×10^{40}	4.6×10^{44}	8.5 ± 0.08^e	634	0.12
PG 2214+139	0.0658	14.7	−22.6	1.21×10^{42}	2.11×10^{40}	2.4×10^{44}	8.6 ± 0.09^e	299	0.06

[a]Uncertainty is ±0.2.

[b]PAH and [Ne II] 12.8 μm luminosities from the *Spitzer* spectra of Schweitzer et al. (2006); estimated uncertainties are 30 per cent.

[c]FIR 10–1000 μm luminosity reported by Haas et al. (2003), except for PG 2214+139, where we use the value reported by Ho (2005). All values have been converted to the luminosity distances adopted here.

[d]Black hole masses from Kaspi et al. (2000). These determinations rely on the Hβ lines with characteristic broad-line region radii based on time lags measured for individual objects by reverberation mapping.

[e]Black hole masses from Vestergaard & Peterson (2006). These determinations rely on the Hβ lines with characteristic broad-line region radii inferred from the continuum luminosity.

[f]The luminosity distance.

[g]The physical plate scale of the images.

Table 2. Filters and exposure times [a]

Object	WFPC2					NICMOS	
	[O II]	Hβ	[O III]	Optical Cont.	[O III] Cont.	Paα	IR Cont.
PG 0026+129	*FR418N* 4620	*FR533N* 3000	*FR533N18*[b] 2400	*F467M* 184	*F588N*[b] 240	*F215N* 2112	*F237M* 144
PG 0838+770	*FR418N* 3400	*FR533N18* 800	*FR533N18* 800	*F467M* 80	–	*F212N* 2112	*F237M* 336
PG 1244+026	*FQUVN* 2240	*FR533N* 920	*FR533N* 1200	*F467M* 240	–	*F196N* 1984	*F222M* 288
PG 1307+085	*FR418N* 1840	*FR533N18* 820	*FR533N33*[b] 1500	*F467M* 400	*F588N*[b] 240	*F216N* 2048	*F237M* 224
PG 1448+273	*FQUVN* 3800	*FR533P15* 3600	*FR533P15* 1760	*F467M* 320	–	*F200N* 2048	*F222M* 240
PG 1613+658	*FR418P15* 1380	*FR533N18* 440	*FR533N18* 440	*F467M* 240	–	*F212N* 2112	*F237M* 288
PG 1626+554	*FR418N* 6100	*FR533N18* 1660	*FR533N33* 1800	*F467M* 320	–	–	–
PG 2214+139	*FQUVN* 1800	*FR533P15* 2840	*FR533P15* 1300	*F467M* 320	–	*F200N* 1824	*F222M* 192

[a]The exposure time is given below each filter in seconds.

[b]These data were first presented in Bennert et al. (2002).

to the failure of the NICMOS instrument, PG 1626+554 was not observed in the near-IR. To obtain the optical continuum images of our targets, we observed each of them in the *F*467*M* filter. This filter covers a region of the continuum free of strong emission lines between the [O II]λ3727 and Hβ lines and provides suitable continuum measurements for both lines.

Because our targets are located at redshifts ≈0.1, the plate scales of our images are typically 2 kpc → 1 arcsec. At this scale, these quasar host galaxies are generously contained within the fields of view of the PC, WF2-4, NICMOS2 and NICMOS3 detectors (36 arcsec×36 arcsec, 80 arcsec×80 arcsec, 19.2 arcsec× 19.2 arcsec and 51.2 arcsec×51.2 arcsec, respectively).

Additionally, we observed the star GS 60200264 as a PSF template in a number of the filters. Due to the large number of filters used in this project, we could not observe the PSF star in each of the filters in which we observed the quasars; in some cases the PSF star was only observed in a filter close to the wavelength range used for a quasar. The observation dates for the PSF star images used with each of the quasar images are also listed in Table 3.

The PC, WF, NICMOS2 and NICMOS3 detectors have plate scales of 0.0455 arcsec, 0.0995 arcsec, 0.0756 arcsec and 0.202845 arcsec, respectively, leaving the PSF of the *HST* under-sampled in all of our images. Sub-pixel dithering allows the recovery of some of this lost angular resolution using the method described in Fruchter & Hook (2002) and Koekemoer et al. (2003). We broke up each of our observations, both of the quasars and of the PSF star, into sub-exposures dithered by sub-pixel amounts using the default WFPC2-BOX pattern. This is a standard dither pattern with

Table 3. Quasar and PSF star observation dates.

| Object | WFPC2 | | | | NICMOS | | |
	[O II]	Hβ	[O III]	Optical Cont.	[O III] Cont.	Paα	IR Cont.
PG 0026+129	2008-06-12	2008-06-12	2000-05-24[a]	2008-06-12	2000-05-24[a]	2008-07-12	2008-07-02
PG 0026+129 PSF	2007-09-18	2007-09-19	2007-09-19	2007-09-19	2007-09-19	2008-07-12	2008-07-02
PG 0838+770	2007-11-25	2007-11-25	2007-11-25	2007-11-25	–	2008-08-08	2008-08-08
PG 0838+770 PSF	2007-09-18	2007-09-18	2007-09-18	2007-09-18	–	2008-07-02	2008-07-02
PG 1244+026	2008-05-13	2008-05-13	2008-05-13	2008-05-13	–	2008-05-15	2008-05-15
PG 1244+026 PSF	2007-09-18	2007-09-18	2007-09-18	2007-09-18	–	2008-07-02	2008-07-02
PG 1307+085	2008-01-21	2008-01-21	2000-03-14[a]	2008-01-21	2000-03-14[a]	2008-02-27	2008-02-27
PG 1307+085 PSF	2007-09-18	2007-09-18	2007-09-18	2007-09-18	2007-09-18	2008-07-02	2008-07-02
PG 1448+273	2007-12-18	2007-12-18	2007-12-18	2007-12-18	–	2008-07-08	2008-07-08
PG 1448+273 PSF	2007-09-18	2007-09-19	2007-09-18	2007-09-19	–	2008-07-02	2008-07-02
PG 1613+658	2008-04-20	2008-04-20	2008-04-20	2008-04-19	–	2008-04-21	2008-04-21
PG 1613+658 PSF	2007-09-18	2007-09-18	2007-09-18	2007-09-18	–	2008-07-02	2008-07-02
PG 1626+554	2007-09-12	2007-09-12	2007-09-18	2007-09-12	–	–	–
PG 1626+554 PSF	2007-09-18	2007-09-18	2007-09-18	2007-09-18	–	–	–
PG 2214+139	2008-07-12	2008-07-12	2008-07-12	2008-07-12	–	2008-06-03	2008-06-03
PG 2214+139 PSF	2007-09-18	2007-09-19	2007-09-18	2007-09-19	–	2008-07-02	2008-07-02

[a]These data were first presented in Bennert et al. (2002).

half-pixel sampling in both directions in the PC and WF detectors, and with dithers that are large enough to optimize hot pixel and bad column rejection while minimizing the field-of-view loss. In all cases the sub-exposures were combined using the MULTIDRIZZLE software package described in Section 3.1 and in Fruchter & Hook (2002) and Koekemoer et al. (2003).

3 REDUCTION OF IMAGES

In addition to providing the raw data, STScI also processes WFPC2 data through a standard calibration pipeline[1]. For this project, we chose to use the data products calibrated by this pipeline, after verifying that the reduction steps were suitable for our purposes. In most cases, this pipeline performs bias subtraction, dark subtraction, shutter correction and flat-field division, and writes photometric keywords to the image headers. The ramp filter images are an exception to this; prior to 2009, ramp filter images were not flat-fielded by the standard pipeline. Following the instructions given by the instrument team[2], we multiplied our ramp filter images by a flat-field image taken in a nearby narrow- or medium-band filter. In practice, the narrow- or medium-band filters with wavelengths closest to those used by our ramp filter observations were the *FQUVN* and *F*467*M* filters.

The STScI pipeline is not, however, able to correct for the charge transfer inefficiency in the WFPC2 instrument. The visible effect is that bright sources have a comet-like streak in the direction of charge transfer; this direction is different for different detectors, but remains the same between sub-exposures. This phenomenon is well documented (Whitmore & Heyer 1997; Whitmore, Heyer & Casertano 1999), but cannot be corrected in images. Instead, we note with an arrow the orientation of the streak in all of our images to avoid confusion with morphological features. Additionally, all of

the image processing steps described in Sections 4, 6 and 7 were designed to exclude pixels within a 5° sector around the streak.

STScI provides an analogous pipeline for NICMOS data[3]; we chose to use post calibrated NICMOS data as well. This pipeline performed the bias subtraction, dark subtraction and flat-fielding, computed the noise and data quality images, and added photometric keywords to the image header. The only additional calibration step that we performed was removing the time variable quadrant bias or pedestal effect from the images using the 'PEDSKY' software (see footnote 3) provided by STScI. This effect is constant within a quadrant but varies from one readout to the next in an unpredictable way; it can be effectively removed using 'PEDSKY'.

With the images reduced, the only processing step that remained before PSF subtraction was combining of the dithered sub-exposures, which we describe below.

3.1 MultiDrizzling

As noted above, to improve the sampling rate of the final images, the observations were dithered by sub-pixel increments, and the calibrated data products were combined using the MULTIDRIZZLE software provided by STScI (Fruchter & Hook 2002; Koekemoer et al. 2003). MULTIDRIZZLE attempts to regain the sampling of the *HST* PSF lost because of the large pixels of WFPC2. Optimally, MULTIDRIZZLE combines sub-exposures at a sampling rate of twice their intrinsic pixel scale. For example, the PC detector has a pixel scale of 0.0455 arcsec per pixel (see footnote 1). MultiDrizzling PC images taken with the correct drizzling pattern would allow one to create images with a pixel scale of approximately 0.02 arcsec per pixel.

Our WFPC2 data include images taken with the PC detector as well as all three of the WF detectors [0.0995 arcsec per pixel (see footnote 1)]; our NICMOS data were taken with NICMOS2 [0.075 arcsec per pixel (see footnote 3)] and NICMOS3 [0.20 arcsec per pixel (see footnote 3)]. Each set of sub-exposures was drizzled

---

[1] WFPC2 instrument handbook: http://www.stsci.edu/instruments/wfpc2.
[2] *HST* Calibration of LRF data:http://www.stsci.edu/hst/wfpc2/analysis/lrf_calibration.html.

[3] NICMOS Instrument Handbook: http://www.stsci.edu/hst/nicmos/documents/handbooks/.

more than once at different sampling rates (i.e. pixel scales) to produce different drizzle products that we use at different stages of the analysis. Experimentation with PSF subtraction (see Section 4) suggested that the most accurate PSF estimation was achieved with each image drizzled to the angular resolution of the detector from which it came. For instance, NICMOS images drizzled to the resolution of the PC detector are oversampled by a factor of 2–4, yielding spurious brightness gradients and miscalculated PSF scalefactors. With the PSF scalefactors calculated using images drizzled to their native resolutions, each image was then redrizzled to the resolution of the PC detector for systematic comparison (see Section 6).

One of the most crucial parts of this work was the PSF scalefactor determination (described below in detail in Section 4). Because the light profile of a typical galaxy at $z \approx 0.1$ is only slightly broader than the WFPC2 PSF, it is essential that the sub-exposures be aligned with extreme precision. Any misalignment will result in artificial broadening of the quasar PSF. To achieve this end, we ran MUL-TIDRIZZLE iteratively every time we produced a drizzle product. In each iteration the sub-exposures were drizzled, the centroids of the quasars in the separately drizzled images were checked, corrections were made to the astrometry and the images were drizzled again. This cycle was repeated until all the centroids fell within 10^{-3} pixels of their target coordinates. Experimentation showed that the PSF subtraction was far more effective using these drizzle products than using products drizzled only once. Below we describe in detail the procedures we used to determine the PSF scalefactor and remove the unresolved quasar light from the image of the host galaxy.

With the multidrizzling complete, the image processing steps were concluded, allowing the subtraction of the PSF of the quasars from the combined images.

4 PSF SUBTRACTION

Historically, different methods have been used to correctly map the normalized *HST* PSF. Bahcall et al. (1997) and McLeod & McLeod (2001) observed a field star and used that as a PSF template. Bennert et al. (2002) did the same, but also used continuum images of the quasars themselves as the PSF template in some cases. This approach was motivated by the realization that the quasar-to-galaxy contrast is so high in the continuum that rescaling the Bahcall et al. (1997) continuum images to the shorter exposure times used in Bennert et al. (2002) left essentially quasar-PSF-only images with very little light from the host galaxy. Both of these methods have the significant advantage that they exactly map the *HST* PSF at the same epoch and detector position of the quasar observations, rather than relying on theoretical PSF models. For this reason, we also observed a PSF star in many of the ramp and narrow-band filters in which we made quasar observations, and we observed each quasar in a continuum filter in the optical and near-IR.

Earlier works (e.g. Bahcall et al. 1997) iteratively align and scale the PSF images in a three parameter fit: an x-axis alignment, a y-axis alignment and a PSF intensity scale factor. As described above, our iterative drizzling ensures that the PSF image as well as the quasar image are aligned with the image centres. This leaves the PSF scalefactor as the only undetermined parameter.

The decomposition of the observed light profile is represented in the upper half of Fig. 1 with a schematic quasar PSF, host galaxy and combined (observed) light profile. The goal of this processing step is to find a scalefactor that rescales the model (star) PSF to match the height of the quasar PSF component of the observed quasar image. The primary challenges are that the relative contributions of the quasar PSF and the galaxy light profile are not known a priori,
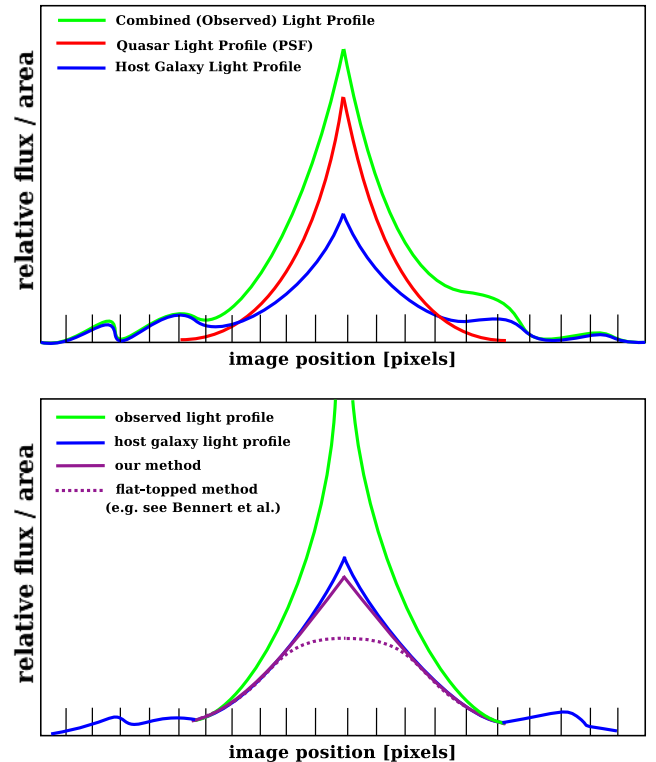
Figure 1. A sketch illustrating the methods for PSF subtraction discussed in Section 4. Top: the radial light profile of a quasar plus host galaxy is compared to its two components, the quasar PSF and the underlying galaxy light profile. The galaxy light profile is broader, which is the basis of the PSF removal method we have devised and describe in Section 4. In practice the contribution from the quasar to the light at the centre of the image can be up to 10 times higher than that of the host galaxy. Bottom: the galaxy light profile from the top figure is compared to the best estimates derived using the two different PSF subtraction methods, the method devised in this work, and the method described in Bennert et al. (2002) and also used by other authors. The method assumes that the light profile of the host galaxy is flat-topped.

and that the width of the WFPC2 PSF is only slightly sharper than the expected typical galaxy profile at $z \approx 0.1$.

Determining the scalefactor with absolute certainty without prior knowledge of the galaxy light profile is impossible. Instead, the best solution is to make as few assumptions about the galaxy light profile as possible, and use those assumptions to place a lower limit on the galaxy luminosity. Utilizing the fact that the central black holes that power quasars are found in the nuclei of galaxies, Bennert et al. (2002) assume that the galaxy light profile decreases monotonically outwards in the central few pixels around the quasar PSF; their residual light profiles may not have a central, local minimum.

The limiting case imposed by this assumption is a flat-topped profile. To achieve this limiting case, Bennert et al. (2002) adopt a scalefactor which makes the central pixel in the residual image have the same value as the average of the surrounding pixels. McLeod & McLeod (2001) make the same basic assumption, that the galaxy's light profile must decrease monotonically, and they construct a model of a quasar PSF + host galaxy, which they fit to the data. In these cases the residual (galaxy) image after PSF removal is a lower limit on the galaxy flux; if the PSF scalefactor were increased, it would violate the monotonicity condition.

In this work. we present a PSF subtraction method which also yields a lower limit on the galaxy flux, but which comes closer to

the true galaxy light profile than the methods presented in Bennert et al. (2002) and McLeod & McLeod (2001). We assume that the underlying galaxy light profile is cuspy; that is, as one moves away from the centre, the post-subtraction residual descends no more rapidly than it did in more central pixels. Essentially, we assume that absolute value of the first derivative decreases moving outward from the centre of the light profile. The PSF scalefactor used for each of the quasar images is the value which just guarantees that this constraint of cuspiness is enforced. This method is graphically represented in the sketch of Fig. 1.

The assumption that the light profiles of the centres of our galaxies are cuspy is well justified by the radial light profiles of nearby galaxies; Lauer et al. (2005) find that 'Nuker' light profiles fit a broad range of galaxies, even galaxies with core profiles in their centres. For all the Nuker-law parameters that Lauer et al. (2005) report, the radial flux profiles have positive second derivatives. Our method would break down for an extreme morphology, such as the interacting and double nuclei objects reported in Disney et al. (1995) and Bahcall et al. (1997), but to visual inspection none of our objects fall into this category.

To compute this scalefactor, we first compute a numerical radial second derivative for each location in the quasar+galaxy and the corresponding derivative in the PSF star image. The desired PSF scalefactor is then just the ratio of the second derivative in the quasar+galaxy image to the second derivative in the PSF star image. In this manner, we construct the PSF scalefactor for each radial direction. Then, we characterize this population of potential scalefactors with a median and a standard deviation around the median. We adopt the median minus the standard deviation as our chosen scalefactor; by choosing the scalefactor in this manner we obtain the lowest upper limit on the scalefactor, hence a lower limit on the flux of the host galaxy light. We then adopt the standard deviation around the median as the uncertainty in the scalefactor.

Our results are shown graphically in Fig. 2, which displays a gallery of azimuthally averaged light profiles of quasars prior to PSF subtraction, their corresponding PSF stars, and the residual light profiles. The light profiles of the quasars before PSF subtraction are only slightly broader than the profiles of the PSF stars. The key element of our technique is visible in lack of inflection points in the residual light profiles; that is, they do not flatten near their centres.

Of course, star-forming clumps, spiral arms or any other lumpiness in the light profile would cause a galaxy to violate this condition at some point. For this reason, the cuspiness condition is imposed only in the central portions of the galaxy where the light profile is likely to be dominated by a combination of a bulge and, in the case of late-type galaxies, an exponential disc. The best estimate of the sizes of quasar host bulges comes from McLeod & McLeod (2001), who deconvolved their quasar/galaxy pairs with a least-squares fit that included an exponential profile to account for the bulges of their galaxies. They find scale radii that range from 0.5 to 1.5 kpc with an average of 1.0 kpc (excluding their one object with uncertain detection). We only demand that the cuspiness condition be satisfied within a radius of three pixels from the centre of the object. This corresponds to a radius of 0.73 kpc for the nearest quasar (PG 2214+139) in the coarsest camera (NICMOS3). Disc-bulge or disc-dominated galaxies present even less of a challenge since their light profiles are shallower. Thus, in all cases our cuspiness condition only is imposed in areas of the galaxy expected to be dominated by regular cuspy morphology.

Additionally, we also note here that pixels in the quasar image and the PSF star image within the 5° sector affected by charge transfer inefficiency (described in detail in Section 3 were excluded from the PSF scalefactor calculation.

Having observed both PSF stars and quasar continuum images, we experimented with both types of PSF templates. Our experiments showed that the PSF star images consistently produced superior results. In particular, while the PSF-subtracted images produced with these two different templates were qualitatively similar, the use of the quasar continuum images as PSF templates is more prone to overestimate the PSF scalefactor, as evidenced by large areas of negative pixels. This result is not surprising given that we detect the host galaxies even in the continuum images (see Section 9 for details of the detections), indicating that the continuum-image light profiles are broader than, and thus poor analogues for, quasar PSFs themselves.

PSF-subtracted images of each of our quasar host galaxies in each of the filters used are shown in Fig. 3. In Table 4, we list the luminosity corresponding to the PSF (unresolved) that we subtracted from each quasar in each filter. In Section 8.1, we compare these luminosities with measurements from ground-based spectra as a consistency check.

5 ARTIFICIAL GALAXY SIMULATIONS

As seen in Fig. 3, the PSF subtraction technique described above produces visually plausible galaxy residuals. Nevertheless, visual inspection is, by itself, an insufficient diagnostic. Because the quasar is so much brighter than the galaxy (Bahcall et al. 1997; McLeod & McLeod 2001; Bennert et al. 2002), especially in the central pixels of the optical images, there is typically a wide range of PSF scale values that produce visually and physically plausible residuals.

To this end, we repeated the PSF subtraction procedure, described above in Section 4, with 2000 simulated quasar+galaxy images in each of the continuum filters, 1000 using an observed PSF star image as a template and 1000 using an artificial PSF generated using Tiny Tim (Krist 1995). In each simulation, we constructed an image by combining a quasar PSF component and a galaxy component (described in detail below), varying the quasar and galaxy brightness and galaxy morphology over the range of physically plausible values to ensure that our technique is applicable over a range of parameters that bracket our eight objects. Then, we verified our technique by applying it to the artificial images and comparing the PSF scalefactor computed using our method to the scalefactor used to generate the images.

The primary component of our simulated data are the light profiles of the quasars themselves. For this, we used an image of the PSF star in the WFPC2 and NICMOS filters rescaled to a magnitude chosen randomly from the range of actual magnitudes of the quasars in Johnson filters similar to the filters used for our continuum observations. The quasars in our sample range from Vega magnitude 14.5 to 16.5 in the *B* filter, so we adopted that as the range for the simulated quasars in the WFPC2 *F*467*M* filter. Similarly, our quasars range from Vega magnitude 14 to 15.5 in the *K* filter, so we adopted that range for our simulated quasars in the NICMOS2 *F*237*M* and NICMOS3 *F*222*M* filters.

We used the IRAF task 'mkobjects' to generate artificial galaxy light profiles. The 'mkobjects' task allows the user to vary the functional form of the light profile, as well as a range of light profile parameters, such as scale radius, ellipticity, position angle and overall brightness. To ensure that this technique is effective for all reasonable galaxy profiles, we varied the profile parameter values over ranges large enough to encompass all likely possibilities.

PG 0026+129

PG 0838+770

PG 1244+026

PG 1307+085
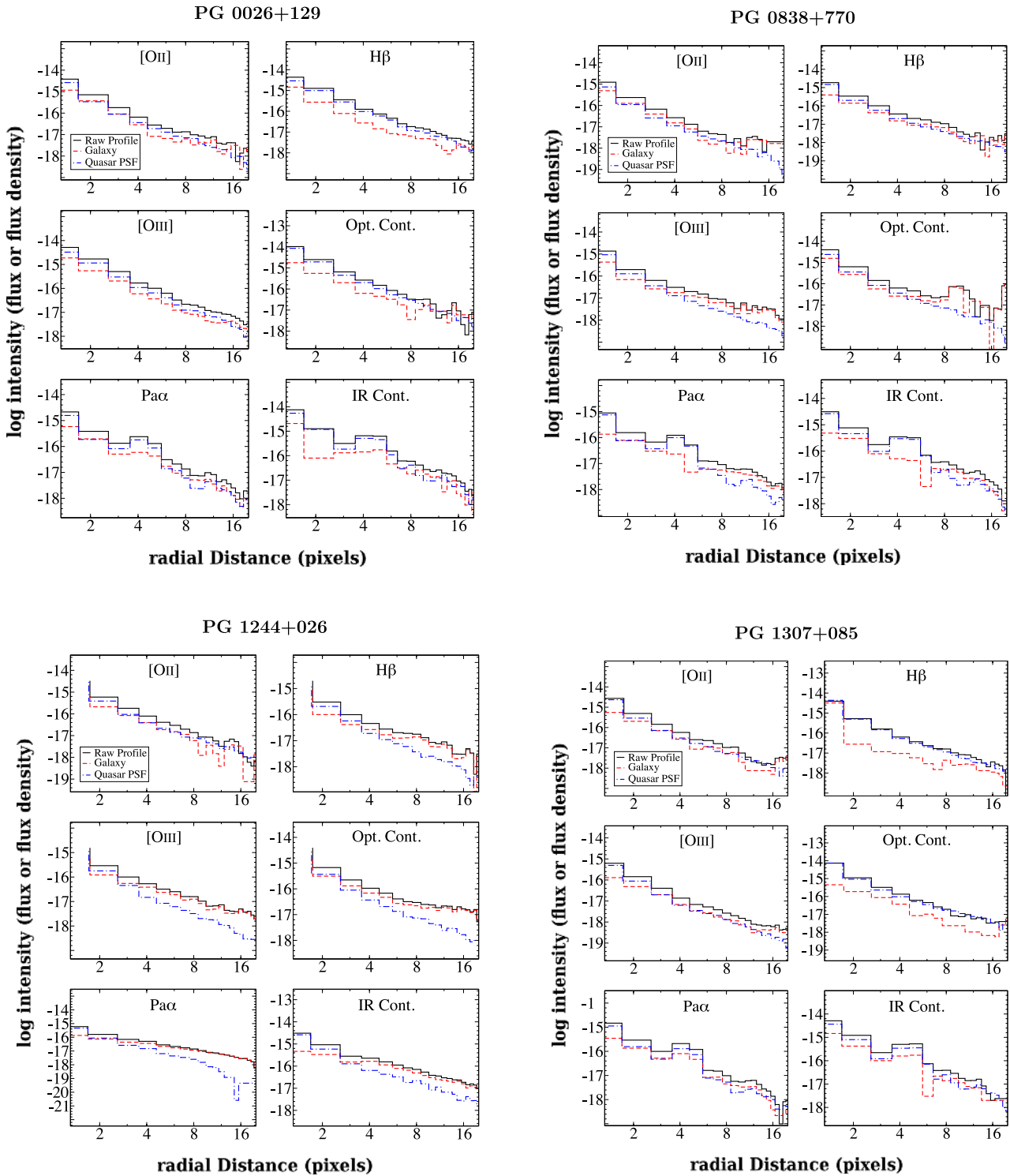
Figure 2. (a) Azimuthally averaged light profiles of the PG 0026+129 host galaxy at each wavelength of interest (black, solid), the corresponding quasar PSF, i.e. the rescaled profile of a PSF star (blue, dot–dashed) and the residual galaxy after PSF subtraction (red, dashed). The azimuthal averaging excludes regions affected by the readout streak in all images involved (see discussion in Section 4). (b) Same Fig. 2(a) but for PG 0838+770. (c) Same Fig. 2(a) but for PG 1244+026. (d) Same Fig. 2(a) but for PG 1307+085. (e) Same Fig. 2(a) but for PG 1448+273. (f) Same Fig. 2(a) but for PG 1613+658. (g) Same Fig. 2(a) but for PG 1626+554. Note the infrared images are missing due to the failure of the NICMOS instrument. (h) Same Fig. 2 a but for PG 2214+139.

For this work, we created galaxies with both exponential disc and de Vaucouleurs (de Vaucouleurs 1959) profiles superimposed on each other to simulate the bulges and the discs of host galaxies. We varied the intensities of the bulge and disc components, ranging

from bulge-dominated galaxies (ellipticals, the most likely quasar host morphology) to disc-dominated galaxies.

We varied the scale radius for the bulge of each galaxy over the range that is physically plausible. For our most distant quasar,
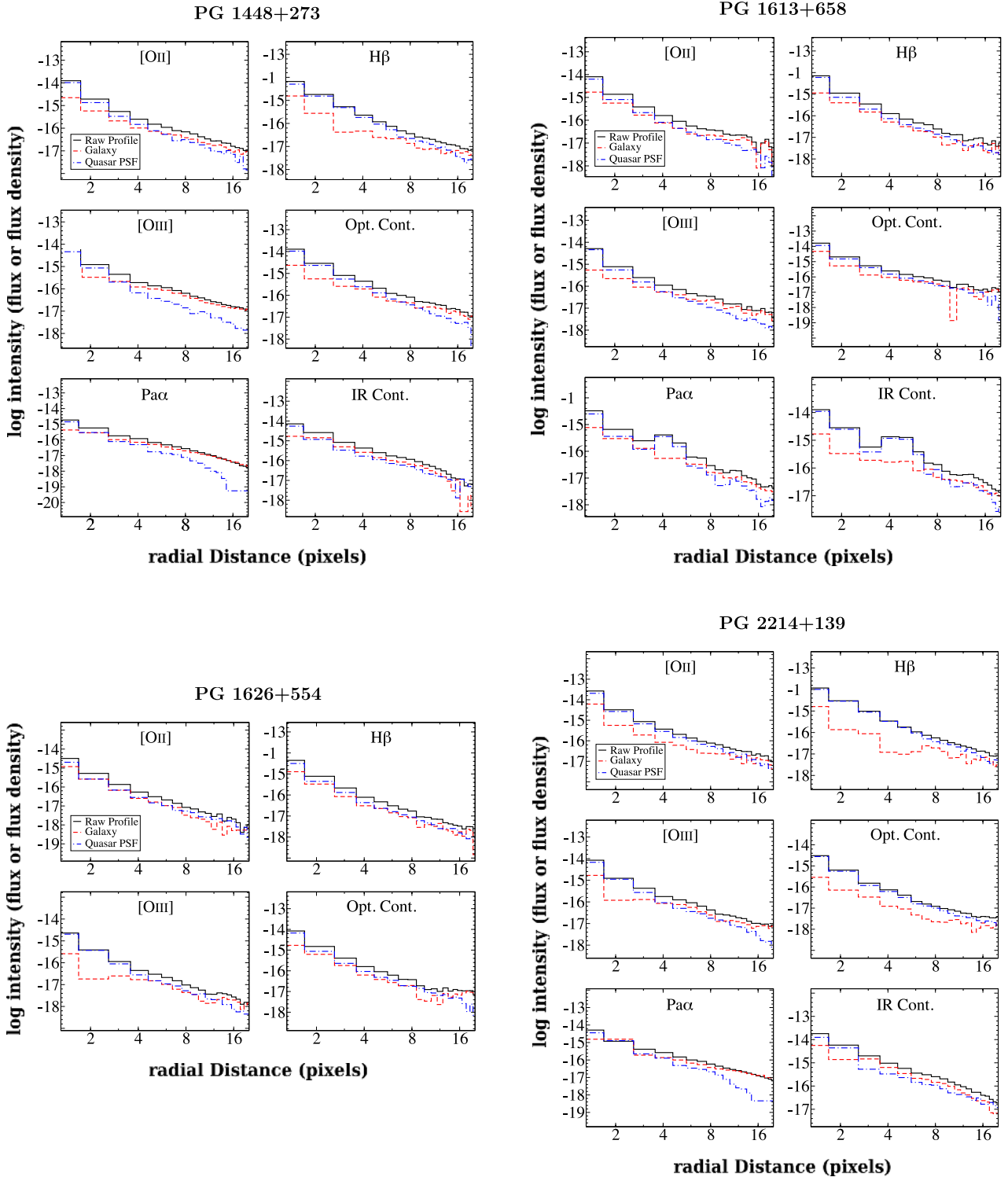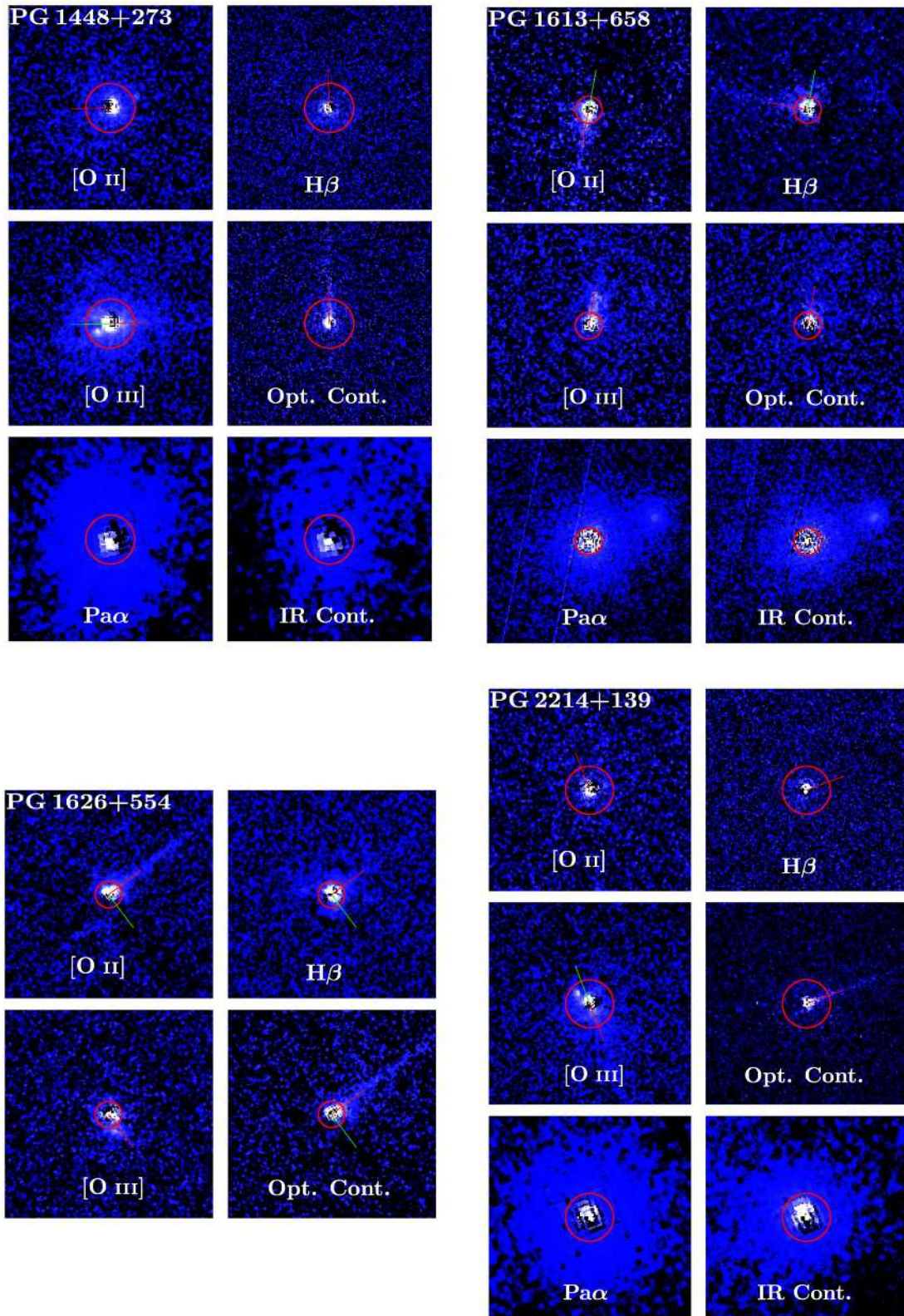
Figure 2 – *continued*

PG 1307+085, seven pixels on the PC detector corresponds to 0.9 kpc; for our nearest quasar, PG 1244+026, 250 pixels on the PC detector corresponds to 10.3 kpc. Therefore, we chose 7 to 250 pixels as the range for the scale radii of the bulges of our simulated galaxies. The disc component was assigned a scale radius randomly in the range from one half to twice the scale radius of the bulge. The axis ratio of the bulge was chosen randomly between 0.6 and 1,

and for the disc between 0.3 and 1. The position angle of the bulge and the disc were chosen randomly but were always equal (i.e., they were always aligned).

Our analysis presented in Section 7 indicates that the dominant source of noise in these high surface brightness regions is source photon counting noise rather than sky or read noise. To emulate this, 'mkobjects' employs a stochastic algorithm
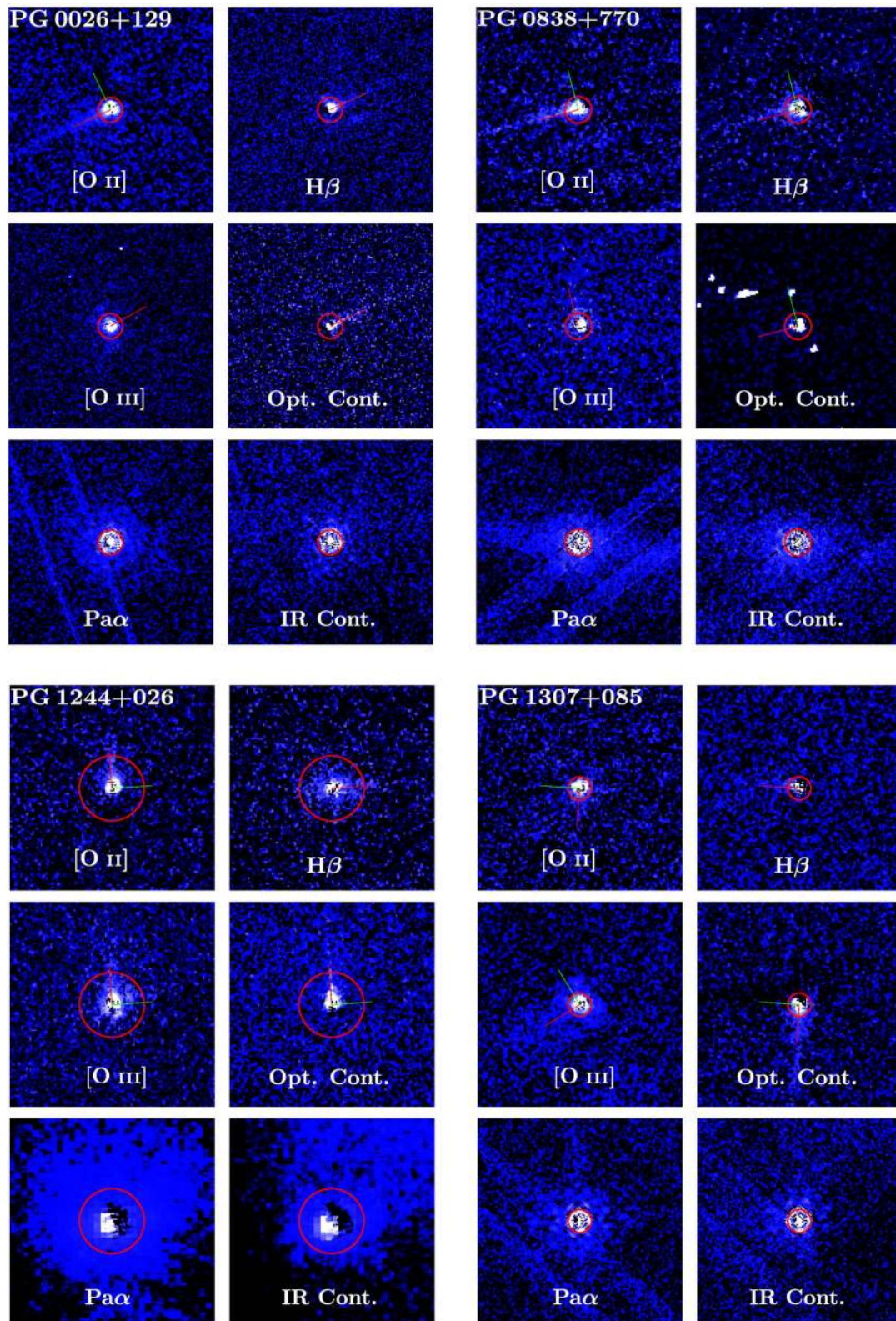
Figure 3. (a) PSF-subtracted images of PG 0026+129 in each of the filters used. The red circle has a radius of 1 kpc at the distance of the quasar. Each tile is 7.5 arcsec×7.5 arcsec. The red line indicates the direction of the WFPC2 streak in the quasar images. The WFPC2 streak in the PSF images often aligns with the streak in the quasar images; when otherwise, it is indicated by a green line. The brightness scale is linear and has been adjusted separately for each panel to bring out faint morphological features. (b) Same Fig. 3(a) but for PG 0838+770. (c) Same Fig. 3(a) but for PG 1244+026. (d) Same Fig. 3(a) but for PG 1307+085. (e) Same Fig. 3(a) but for PG 1448+273. (f) Same Fig. 3(a) but for PG 1613+658. (g) Same as Fig. 3(a) but for PG 1626+554. Note the infrared images are missing due to the failure of the NICMOS instrument. (h) Same Fig. 3(a) but for PG 2214+139.

Figure 3. – *continued*

which ensures that the images are not just perfectly smooth light profiles.

The bulge magnitude of each simulated galaxy was set based on its simulated quasar's magnitude. First, we assume that the central black holes are accreting at the Eddington limit. Although the accretion rate can be substantially smaller, the Eddington limit represents a pessimistic scenario for the PSF subtraction because it results in a low galaxy-to-quasar contrast. Next, we connect the black hole mass

Table 4. Quasar-only (PSF) line and continuum luminosities.[a]

Object	L(line)(10^{40} erg s^{-1})				L_λ(cont.)(10^{40} erg s^{-1} Å^{-1})	
	[O II]	Hβ	[O III]	Paα	B	IR
PG 0026+129	211 ± 6	321 ± 6	370 ± 20	124 ± 2	10.3 ± 0.5	0.97 ± 0.03
PG 0838+770	61 ± 2	87 ± 2	67 ± 3	60 ± 1	2.7 ± 0.1	0.47 ± 0.01
PG 1244+026	21.8 ± 0.6	12.6 ± 0.7	9.1 ± 0.5	2.21 ± 0.04	0.36 ± 0.01	0.0303 ± 0.0004
PG 1307+085	197 ± 7	318 ± 5	39 ± 1	133 ± 4	7.2 ± 0.2	0.94 ± 0.03
PG 1448+273	178 ± 5	97 ± 2	70 ± 1	8.2 ± 0.1	2.2 ± 0.1	0.122 ± 0.001
PG 1613+658	360 ± 10	297 ± 7	258 ± 8	188 ± 4	9.8 ± 0.2	1.97 ± 0.03
PG 1626+554	139 ± 6	197 ± 6	137 ± 3		5.3 ± 0.1	
PG 2214+139	293 ± 7	179 ± 9	100 ± 2	58.7 ± 0.8	0.59 ± 0.04	0.428 ± 0.006

[a] Derived from the portion of the quasar+galaxy light removed by PSF subtraction.
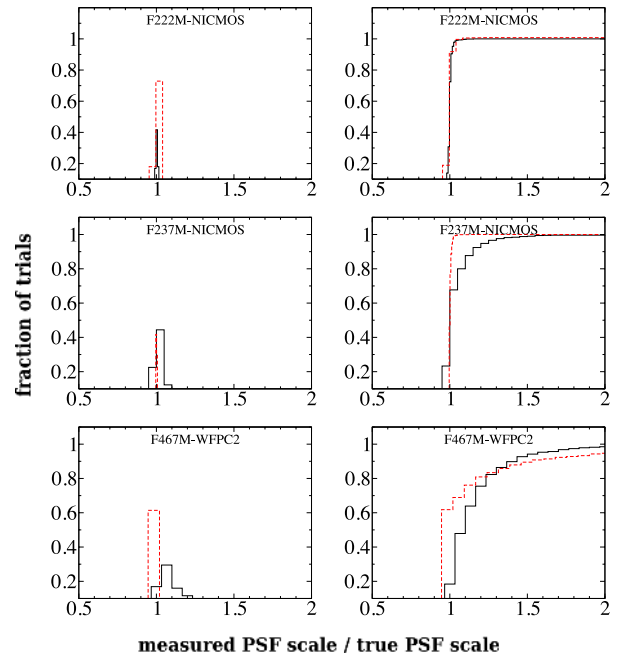
to the spheroid magnitude using known central black hole mass to host spheroid magnitude relations (Bettoni et al. 2003) and a 'standard' quasar SED[4]. Then, a uniform random number from −1 to 1, based on the rms scatter in the Bettoni et al. (2003) relationship, was added to the bulge magnitude to simulate actual scatter in the relation between quasar magnitude and bulge magnitude. Finally, the galaxy disc magnitude was set to be the bulge magnitude plus a uniform random number from −1 to 1. Thus, our simulated galaxies range from bulge-dominated to disc-dominated systems, in keeping with the observed properties of quasar host galaxies (McLeod & McLeod 2001; Guyon et al. 2006).

We applied the PSF subtraction procedure, described in Section 4, to our simulated quasar+galaxy light profiles. In this analysis, the quantity of merit is the ratio of the PSF scalefactor, computed using the method described in Section 4, to the true scalefactor, seeded into the simulated image. In Fig. 4, we plot histograms of this ratio for the three continuum filters used (WFPC2 *F*467*M*, NICMOS2 *F*237*M* and NICMOS3 *F*222*M*). These histograms peak strongly around a value of unity, indicating that in most of the simulations this procedure comes very close to recovering the true PSF scalefactors.

There are two ways that a poorly estimated PSF scalefactor can impact our results. Primarily, since underestimated scalefactors cause PSF light to remain in the residual image, a severely underestimated scalefactor could result in a false detection. We estimate our galaxy detection confidence from the median value of the underestimated scalefactors (ratios less than one): 0.99, 0.99 and 0.98 for the *F*222*M*, *F*237*M* and *F*467*M* images, respectively.

Secondarily, an overestimated or underestimated scalefactor affects the apparent brightness of a galaxy. We can estimate the impact that errors in the PSF subtraction have on our photometric measurements from the overall spread in the histograms. Since they are asymmetric with a broader tail towards higher values, we conclude that the primary source of photometric uncertainty is from over subtraction. Given that, we derive our photometric confidence from the median values of the overestimated scale factors, which are 1.006, 1.03 and 1.1 for the *F*222*M*, *F*237*M* and *F*467*M* images, respectively.

We stress here that these uncertainty estimates are worst-case-scenarios because of the assumptions in our simulations, namely Eddington accretion rates and continuum instead of emission-line filters. Therefore, the contribution to the uncertainty for each

---

[4] We have considered the SEDs and bolometric corrections of (Elvis et al. 1994) and (Richards et al. 2006), which yield bolometric luminosities that differ by approximately 17 per cent. This difference is not significant given that we apply a scatter of ±1 mag in the luminosity of the bulge of the host galaxy.

Figure 4. Results of simulations assessing the fidelity of our PSF scaling method. For each of the medium-band, continuum filters, we show the differential (left) and cumulative (right) distribution of ratios of computed to true PSF scalefactors. These distributions are based on 1000 quasar+galaxy simulations using observed PSF stars (plotted in black) and 1000 simulations using synthetic (TinyTim) PSF stars (plotted in red). A value of unity for this ratio indicates that the PSF subtraction algorithm correctly determined the intensity of the quasar PSF. Note that the distributions in all three filters peak around unity, indicating that the algorithm is likely to converge on the right value. For scalefactors using real PSF stars, ratios less than unity, the median values are 0.99, 0.99 and 0.98 for the *F*222*M*, *F*237*M* and *F*476*M* filters, respectively. See Section 5 for a discussion.

real image from the PSF subtraction process is computed on a case-by-case basis based on the statistics of each image, as described in Section 4.

6 ANALYSIS OF HOST GALAXIES AFTER PSF SUBTRACTION

6.1 Continuum subtraction

Because the analysis in the following sections utilizes emission-line strengths and line ratios, it is necessary to remove any stellar

continuum contribution in our PSF-subtracted images. Since the NICMOS continuum filters were chosen to be adjacent to the Paα emission line, the flux density in those images was scaled by the Paα filter width and subtracted from the Paα images.

The optical continuum filter, *F467M*, is not immediately adjacent to the optical narrow-band filters used for the emission-line images ($\delta\lambda/\lambda$ is a factor of 10 larger than for the infrared continuum filters). We use the optical continuum images only as intensity maps for the optical continuum underneath the emission-line flux in the emission-line images. To properly scale the optical continuum images to match the continuum component of the emission-line images, we compute continuum scalefactors by imposing the constraint that there be no negative residuals (to within noise) after continuum subtraction. By scaling up the continuum image as much as possible without creating negative residuals, prior to subtracting it from the emission-line images, we establish a lower limit on the emission-line flux. This technique is robust in the sense that it guarantees that the remaining flux is line emission; however, it is technically a lower limit to the emission-line flux. In practice, the fluxes we report are highly likely to be close to the true values since even before continuum removal there is relatively little flux in at least some areas of each of the host galaxies. We estimate the uncertainty in this continuum-subtraction scalefactor from the background noise in the images, since the noise represents the limit to which we can demand non-negative pixel values. In practice, the continuum contribution, integrated over the area of the host galaxy, was very small in the optical emission-line images, considerably less than 1 per cent on average.

6.2 Extinction correction

To estimate dust extinction, we employed maps of the ratio of Hβ/Paα in the PSF- and continuum-subtracted images to create maps of A_V using the dust extinction law described in Cardelli, Clayton & Mathis (1989), adopting the recommended extinction curve of $R_V = 3.1$. For each pixel that was above the background noise in both the Hβ and Paα images we computed the Hβ/Paα ratio. The background noise was computed as the standard deviation of regions of the image far from even the most extended of our targets and not occupied by known image defects.

The values were then averaged using a circular top-hat kernel (this is the simplest choice of kernel since it weighs all pixels equally). For each pixel in each A_V map, the radius of the kernel was initially set to the size of the pixels of the NICMOS camera used to create the Paα image. For quasars whose Paα image was taken with NICMOS2, this is 1.7 PC-chip pixels; for NICMOS3, 4.6 PC-chip pixels. The kernel was then expanded until the signal-to-noise ratio (S/N) of the average exceeded unity, and the measured Hβ /Paα line ratio was at or below the intrinsic $T = 10\,000$ K value of 2.146 (Brocklehurst 1971). We also rejected pixels in the Hβ image that fell within the 5° sector affected by the charge transfer inefficiency. Although this strategy degrades the angular resolution of the Hβ/Paα map, it is absolutely necessary because the emission-line images, and thereby every measured quantity in the sections that follow, depend on the extinction correction, especially near the heavily extinguished galactic centres.

Maps of A_V for each of the seven objects for which we have NICMOS imaging are shown in Fig. 5. The values of A_V that we find for the centres of our quasars range from 1.1 in PG 0026+129 to 2.7 in PG 1448+273, with a median value of 1.9. We note that that PG 0026+129 is our most luminous quasar, while our least
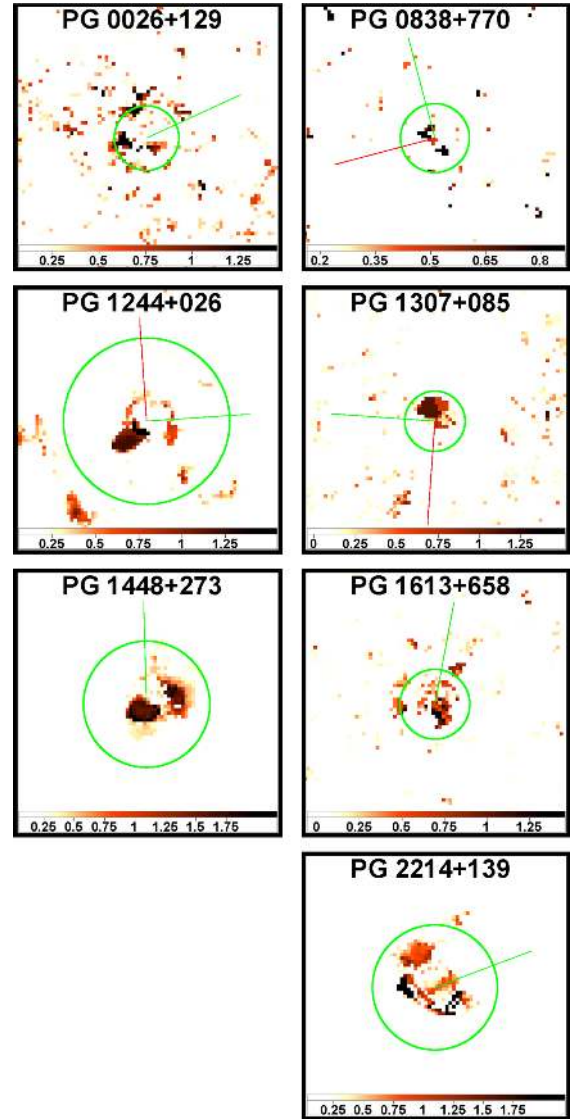
Figure 5. Maps of A_V for the seven of the eight quasars for which we possess both Hβ and Paα images. The green circle marks 1 kpc radius. Each panel is 3.4 arcsec on the side.These maps are derived as described in Section 6.2. Points with uncertainties greater than 0.3 in log–log A_V are excluded.

luminous quasar, PG 1244+026, has the third highest extinction value of 1.7.

Because we were not able to obtain Paα images of PG 1626+554, we resorted to performing extinction correction on the PG 1626+554 images with a typical A_V map produced using the seven quasar hosts for which we posses Paα images. After plotting azimuthally averaged values of A_V against radial distance from quasar centre (in kpc), we determined, by visual inspection, that a typical quasar host had $A_V \approx 0.3$ out to 1 kpc, $A_V \approx 0$ beyond 1.6 kpc, with a linear interpolation between 1.0 and 1.6 kpc. We emphasize here that, for reasons that will be discussed in Section 8.2, assuming a typical A_V map does not significantly impact our line-ratio analysis nor our detection for star-forming regions in PG 1626+554.

7 ANALYSIS OF UNCERTAINTIES

The uncertainty map in each final science image depends on the uncertainty maps of as many as 10 drizzled images, each propagated

through all the processing steps needed to produce the final science images, namely quasar PSF subtraction, continuum subtraction and reddening correction. Prior to any of these processing steps, the typical photometric uncertainties associated with counting statistics are the primary source of uncertainty in the raw images. Our narrow-band space-based observations are relatively background free, making background noise and errors from background subtraction a small component of our net uncertainties. The process of drizzling the raw images creates correlated noise, making simple Poissonian estimators of uncertainties inapplicable. Because the effective exposure time of a pixel in a drizzled image depends on the relative alignments of the undrizzled images, the change in plate scale from before and after drizzling, and the choice of drizzle kernel used, MULTIDRIZZLE produces a weight map which is essentially an exposure time map of the drizzled image (Fruchter & Hook 2002; Koekemoer et al. 2003). Formally, the uncertainty for an image is its variance; in units of counts, the uncertainty is the square root of each pixel value plus the read noise. Since this project's images are in counts-per-second, we assign to each pixel in the uncertainty map the square root of the ratio of that pixel in counts-per-second to the value of the corresponding pixel in the exposure time map, added in quadrature with the read noise, as the value in an uncertainty map image. Quasar-image pixels which are negative have been primarily affected by the read noise; for these pixels, their values in the error map are just the read noise. With the above considerations in mind, we propagated the uncertainties through all the steps of data reduction and ensuing analysis to produce an error map for each image.

The extinction correction is the only processing step for which the propagation of uncertainties was not straightforward. Because each pixel in the A_V map is the result of smoothing with a circular top-hat kernel (see Section 6.2), the uncertainty in A_V is, for most pixels, related to the uncertainty in the average of several values of $H\beta/Pa\alpha$. The uncertainties for each pixel in the A_V map were then propagated to the pixels in the extinction-corrected images through the Cardelli et al. (1989) extinction law and used to compute the uncertainties in final extinction-corrected fluxes.

Of particular interest are the uncertainties on the diagnostic line ratios, [O III]/[O II] and [O III]/Hβ, since these affect our identification of star-forming regions, as well as the uncertainties in the emission-line luminosities, which lead to uncertainties in the SFRs. The uncertainties in the line ratios resulting from a combination of photometric errors and errors in extinction corrections based on the Cardelli et al. (1989) extinction law range between 0.1 and 0.18 dex. The uncertainties in the integrated line luminosities are considerably smaller and do not contribute appreciably to the final uncertainties in the SFRs. We discuss these uncertainties further in Section 8.2 and indicate their magnitude in the relevant figures.

In addition to the photometric uncertainties and the uncertainties in the determination of A_V, there is an additional uncertainty stemming from the lack of knowledge of the extinction law in the centres of quasar host galaxies. While we have adopted the extinction law from Cardelli et al. (1989), we also quantify the impact of this uncertainty on our results in Table 6 by translating our lowest, median and highest central $H\beta/Pa\alpha$ ratios through a number of different extinction laws. In particular, we experimented with the Milky Way extinction laws of Cardelli et al. (1989) and Seaton (1979), the Small and Large Magellanic Cloud extinction laws of Bouchet et al. (1985) and Koornneef & Code (1981), respectively, and the starburst galaxy extinction law for nebular emission lines by Calzetti, Kinney & Storchi-Bergmann (1994). For each law and each value of $H\beta/Pa\alpha$ we report in Table 6 the values of A_V and

$\Delta\log([O III]/[O II])$, the amount by which $\log([O III]/[O II])$ would change as a result of extinction. The quantity of merit in Table 6 is the variation of $\Delta\log([O III]/[O II])$ between extinction laws for a given value of $H\beta/Pa\alpha$. The Cardelli et al. (1989) extinction law, which we adopt here, results in values of A_V and $\Delta\log([O III]/[O II])$ in the middle of the range spanned by all the extinction laws. The maximum variation about the value of $\log([O III]/[O II])$ inferred based on the Cardelli et al. (1989) law is 0.22. Thus, the choice of extinction law has a relatively small effect on the identification of star-forming regions through diagnostic diagrams. We return to these uncertainties in Sections 8.2 and 8.4, where we describe their effect on the derived SFRs.

8 RESULTS

8.1 Comparison of unresolved fluxes to measurements from ground-based spectra

We have compared the emission-line fluxes measured from our images with those measured from spectra taken from the ground. We have used the spectra presented by Boroson & Green (1992), which were taken between 1990 February and 1991 April and cover the rest-frame wavelength range from $H\gamma$ to [O III]λ5007. The spectra were taken through a 1.5 arcsec slit, which encompasses the flux from the extended line-emitting regions that we detect in our images. Accordingly, we have measured the flux in these spectra that falls within the bandpass of the corresponding $H\beta$ and [O III] narrow-band filters and compared it to the total fluxes measured from the images (before PSF subtraction).

The comparison is complicated by the fact that the fluxes measured from the spectra in the narrow filter bands are dominated by the continuum and broad $H\beta$ line, which are variable by a factor of $\sim$2 on time-scales of months to a year. The continuum and broad $H\beta$ line contribute at least 90 per cent of the flux in the $H\beta$ filter while the continuum contributes $\sim$70–90 per cent of the flux in the [O III] filter. Moreover, the broad $H\beta$ flux is comparable to the continuum flux in the $H\beta$ filter and the two do not vary in phase; the broad $H\beta$ variations lag the continuum variations by 1–3 months (Kaspi et al. 2000). In view of the variability, the only meaningful comparison we are able to make is between the ratios of fluxes in the two filters as measured from the spectra and as measured from the images (the sum of the values in Tables 4 and 7). We find that the flux ratios agree to 10 per cent in four objects and to 25 per cent in another two objects. This agreement is reasonable in view of the variability characteristics of the broad $H\beta$ line reported by Kaspi et al. (2000). For the remaining two objects, the [O III] images were taken by Bennert et al. (2002) seven years before our own observations thus allowing continuum variability to distort the flux ratios.

8.2 Line ratios

Using the images of the quasar hosts after continuum subtraction and extinction correction, we characterize the power source of line emission in the host galaxies on a region-by-region basis through the use of emission-line ratio diagnostics. Specifically, we determine whether the line emission in a region is powered by the hard ultraviolet and X-ray flux from the central quasar or the softer ultraviolet flux from young stellar populations (Baldwin et al. 1981; Osterbrock 1989; Netzer et al. 2004) by placing emission from that region in a [O III]/Hβ versus [O III]/[O II] plot in Fig. 6, a variant of the diagnostic line-ratio diagram in figs 1 and 2 of Baldwin et al.
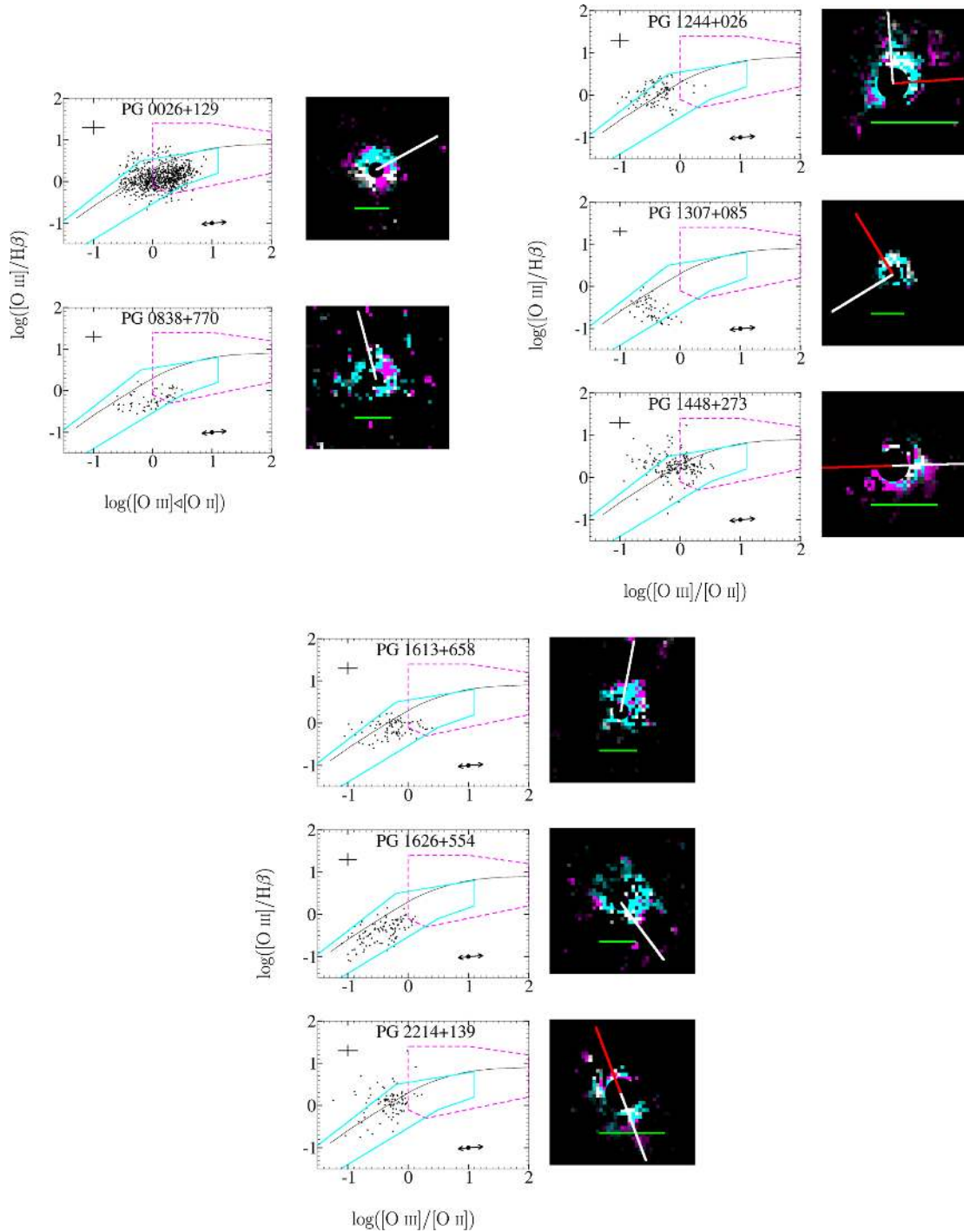
Figure 6. (a) Diagnostic line-ratio diagrams (BPT diagrams, left) and 2 arcsec × 2 arcsec maps (right) for the emission-line regions we detected in the first two object of our sample. In the diagnostic diagrams, we plot a point for each pixel in the line-ratio map (pixels with $S/N < 3$ are excluded from both the diagrams and the maps). The thin, solid, black line shows the H II region according to Baldwin et al. (1981). The thick, solid line (cyan) shows the locus of H II regions according to the models of Dopita et al. (2006) and the compilation of data therein. The thick, dashed line (magenta) is the locus of AGN narrow-line regions based on photoionization models by Groves et al. (2004a,b) and the data compilations of Nagao et al. (2001, 2002) and Groves et al. (2004a,b). In the top left corner of each diagnostic diagram, we plot the median error bar resulting from uncertainties in the photometry and extinction corrections based on the Cardelli et al. (1989) law. In the lower right corner of each diagnostic diagram, we indicate with arrows the maximum possible offsets of points due to different choice of extinction law. More details are given in Sections 7 and 8.2 of the text. Points that fall in the H II region locus of diagnostic diagrams, but not in the AGN narrow-line region locus are coloured in cyan on the maps. Points that fall the in AGN narrow-line region locus of the diagnostic diagram, even if they are in the H II region area are coloured in magenta on the maps. Points that are outside these two areas of the diagnostic diagram are indicated in grey-scale. A filled black circle at the centre of each map indicates the region where PSF subtraction uncertainties are large. The direction of the charge transfer inefficiency streak in the [O III] quasar and PSF images are indicated by white and red bars, respectively, leading away from the centre. The horizontal green bar on each map corresponds to a length of 1 kpc at the distance of the quasar. At least half of the AGN narrow-line region flux is contained within the PSF area and has been subtracted (see Section 8.3 of the text). (b) Same as Fig. 6(a), but for the next three objects. (c) Same as Fig. 6(a), but for the next three objects.

(1981). We combine these with the predictions of recent photoionization models, as we detail below.

In Fig. 6, we show a separate diagnostic diagram for each object in our sample, in which we plot a point for each pixel location in our emission-line images. The thin, solid, black line in each diagram represents the track followed by H II regions according to Baldwin et al. (1981). The area of the diagram bounded by a thick, solid line represents the location of H II regions according to the models of Dopita et al. (2006) and the compilation of data therein. Young H II regions, ≈ 0.2 Myr old, are found at the centre of the diagram while older H II regions, up to ≈ 4 Myr old, are found progressively further from the centre, towards the lower left. The area of the diagram bounded by a thick, dashed magenta line represents the location of AGN narrow-line regions, i.e., those photoionized by a power-law continuum. This area is defined by a combination of photoionization models by Groves et al. (2004a,b), which include the effects of dust and depletion of heavy elements in the gas, and measurements taken from the compilations of Nagao, Murayama & Taniguchi (2001), Nagao et al. (2002) and Groves et al. (2004a,b). These models are also parametrized by the dimensionless ionization parameter, U, which is the ratio of the atomic density to the photon density; we adopt models with $\log U \geq -3$ since these are the models that match the observations. The ionization parameter increases from $\log U = -3$ at the centre of the diagram to $\log U = 0$ at the right edge.

Shown alongside each line-ratio diagram in Fig. 6 is a line-ratio map of the host galaxy. These maps were created by multiplying a grey-scale [O III] image of the host galaxy by the colour corresponding to each pixel's location in the diagnostic diagram. Specifically, points that fall in the H II region area of the diagnostic diagram, but not in the AGN narrow-line region area are in cyan. Similarly, points that fall the in AGN narrow-line region area of the diagnostic diagram, even if they are in the H II region area, are in magenta. Points that are outside these two areas of the diagnostic diagram are indicated in grey-scale. In this manner, we map out the emission-line morphology of each host galaxy.

Points with uncertainties greater than 0.5 in the log of the line ratio were excluded both from the line-ratio diagrams and the line-ratio maps. Pixels that fell within the $5°$ sector of the WFPC2 charge transfer inefficiency streak in either the Hβ, [O II], [O III], or optical continuum image, or any of their respective PSF star images, were not plotted in the diagnostic diagrams, although those pixels are still shaded by the appropriate colour in the corresponding image. In principle, if none of the $5°$ sectors overlapped this could have excluded $40°$ or 11 per cent of the host galaxy image area; in practice, the streaks often overlap, and the largest fraction of excluded area is only 7 per cent.

We plot, in the upper left corner of each diagnostic diagram, median error bars for all the pixels included on the plot. These error bars include contributions from photometric uncertainties and uncertainties in the extinction correction based on Cardelli et al. (1989). The magnitudes of these error bars are listed in Table 5. As we noted in Section 7, the choice of extinction law also results in an uncertainty in the line ratios, with a maximum value of $\Delta \log ([O III]/[O II])$ of 0.22 (see Table 6). We illustrate this uncertainty with a pair of arrows in the lower right corner of each diagnostic diagram. The arrows indicate the maximum shift of the data points (in magnitude and direction) in the diagram resulting from a change in the extinction law. Because the [O III]/Hβ ratio is much less sensitive to extinction than [O III]/[O II], the arrows are approximately parallel to the star-formation tracks. Therefore, the uncertainty arising from the choice of extinction law

Table 5. Median logarithmic error bars on diagnostic emission-line ratios[a].

Object	$\delta \log \left(\frac{[O\,III]}{H\beta} \right)$	$\delta \log \left(\frac{[O\,III]}{[O\,II]} \right)$
PG 0026+129	0.16	0.18
PG 0838+770	0.13	0.13
PG 1244+026	0.16	0.14
PG 1307+085	0.10	0.11
PG 1448+273	0.14	0.17
PG 1613+658	0.13	0.15
PG 1626+554	0.14	0.18
PG 2214+139	0.14	0.18

[a]These error bars capture uncertainties in the photometry and the extinction corrections, assuming the Cardelli et al. (1989) extinction law, but do not include the effect of changing the extinction law. They are shown graphically in the upper left corners of the diagnostic diagrams of Fig. 6. See Sections 7 and 8.2 of the text.

has a relatively small effect in our identification of star-forming regions.

Combining the uncertainties arising from photometric errors and extinction corrections, the error bars on $\log ([O III]/[O II])$ are ≤ 0.25 and the error bars on $\log ([O III]/H\beta)$ are ≤ 0.18. Thus, the combined uncertainties are not large enough to shift a significant number of points out of the locus of H II regions, although they do result in a modest uncertainty in the inferred SFRs, which we quantify in Section 8.4. Moreover, our conclusions with regard to PG 1626+554, the object for which we have not been able to measure extinction values, appear to be robust.

It is noteworthy that in five of our eight quasars, the vast majority of points in the diagnostic diagrams are in the H II region area and not in the AGN narrow-line region area. In the remaining three objects, PG 0026+129, PG 0838+770 and PG 1448+273, about half of the points fall in the overlap between the H II region area and the AGN narrow-line region area, suggesting that we are either observing H II regions distributed *within* the AGN narrow-line region or we are observing star-forming regions only but with a range of ages (i.e., ages that increase towards the centre of the host galaxy). We consider the former interpretation less likely because (a) the candidate AGN narrow-line region pixels correspond to uncharacteristically low values of $\log ([O III]/[O II])$ (the distribution of observed values of $\log ([O III]/[O II])$ for AGN narrow-line regions peaks between 0.4 and 1.0), and (b) the candidate AGN narrow-line region pixels are typically further away from the quasar than the star-forming regions, where the intensity of the ionizing radiation from the quasar is low (the line ratio map of PG 1448+273 in Fig. 6 is a good example). Nonetheless, we take this issue into consideration when we estimate the uncertainties on the SFRs in Section 8.4.

Additionally, we also plot azimuthally averaged (averaged within concentric annuli) line ratios as a function of radius from the centre of each galaxy in Fig. 7. The azimuthal average has the merit of bearing out any radial trends in harder versus softer ionizing radiation with greater S/N than a direct line-ratio map, as in Fig. 6. Our findings based on these figures are also discussed in Section 9.

8.3 The AGN narrow-line regions

The results of the previous section suggest very strongly that the AGN narrow-line regions of our targets are very compact and they are contained within the PSF region that we subtracted, i.e., their

Table 6. Comparison of extinction laws.

| Extinction law | Minimum extinction -0.12 | | Median extinction -0.45 | | Maximum extinction -0.78 | |
	A_V	$\Delta \log \left(\frac{[O\,III]}{[O\,II]} \right)^a$	A_V	$\Delta \log \left(\frac{[O\,III]}{[O\,II]} \right)^a$	A_V	$\Delta \log \left(\frac{[O\,III]}{[O\,II]} \right)^a$
Cardelli[b]	1.1	0.17	1.9	0.3	2.7	0.42
Seaton[b]	1.3	0.12	2.2	0.2	3.1	0.29
SMC[c]	0.78	0.26	1.3	0.45	1.9	0.64
LMC[c]	0.96	0.26	1.7	0.45	2.4	0.64
Starburst[d]	1.4	0.2	2.5	0.34	3.6	0.49

$\log(\frac{H\beta}{Pa\alpha}) =$

[a]The change in the value of $\log([O\,III]/[O\,II])$ for the value of A_V and the extinction law listed.
[b]Milky Way extinction laws by Cardelli et al. (1989) and Seaton (1979).
[c]Small and Large Magellanic Cloud extinction laws by Bouchet et al. (1985) and Koornneef & Code (1981), respectively.
[d]Starburst galaxy extinction law by Calzetti et al. (1994), applicable to the nebular emission lines.
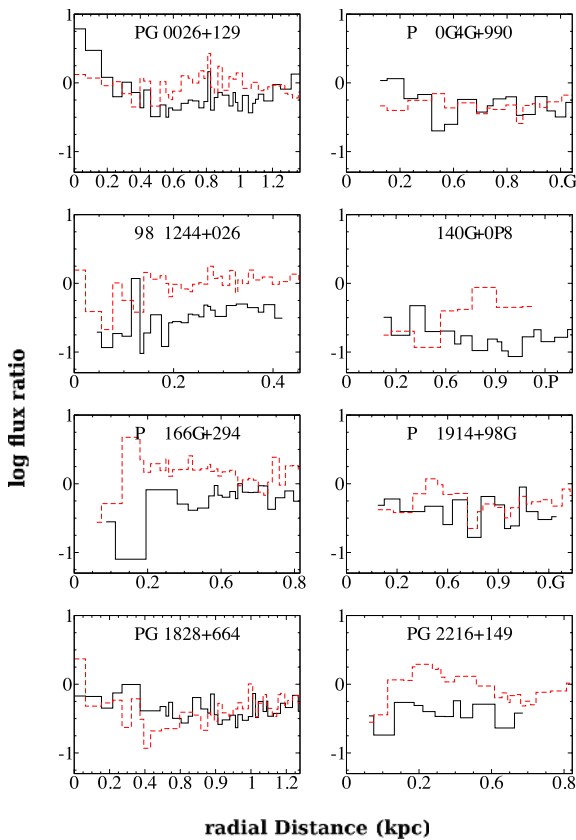
Figure 7. Azimuthally averaged line ratios for the quasar host galaxies, plotted as a function of radius from the centre of the galaxy. The black, solid line represents $\log([O\,III]/[O\,II])$, while the red dashed line represents $\log([O\,III]/H\beta)$. As in Fig. 6(a), $\log([O\,III]/[O\,II]) \gtrsim 1$ near the nucleus indicates the presence of a narrow-line region excited by ionizing photons from the quasar; see Section 8.2 and Baldwin et al. (1981).

extent is a few hundred pc or less. With this in mind, we have estimated the fraction of the $[O\,III]\lambda5007$ flux that falls in the extended emission-line region (reported in Table 7) by comparing it to the total $[O\,III]\lambda5007$ flux measured from the spectra (see Section 8.1). In the process, we have also taken into account the fraction of the extended emission-line flux that can be attributed to star formation (based on the diagnostic diagrams of Section 8.2) and we have assumed that the emission-line flux contained within the PSF can be

ascribed to the AGN narrow-line region. Thus, we find that the AGN narrow-line regions contribute approximately 50–90 per cent of the $[O\,III]\lambda5007$ flux but this fraction should be regarded with caution since the flux measured from the spectrum suffers from uncertain slit losses.

8.4 Star-formation rates

We compute SFRs from the $H\beta$ and $Pa\alpha$ line images. Specifically, we apply the prescription from section 2.3 of Kennicutt (1998, derived for a Salpeter initial mass function (IMF)) to the $H\beta$ and $Pa\alpha$ emission-line luminosities. In the spirit of our discussion in Section 8.2, we compute the star-formation rate using the line luminosity from securely identified star-forming regions and from the total extended line luminosity and we treat these as lower and upper bounds to the SFR. We list the total line luminosities and resulting SFRs in Table 7. For each pixel, the SFR is computed independently from the $H\beta$ and $Pa\alpha$ luminosities. Because the extinction correction forces them to a constant ratio, they are essentially the same measurement; therefore, in most cases they are simply averaged. When they differ by more than their mutual error bars, we defer to the $Pa\alpha$ derived SFR because the $H\beta$ SFRs are more sensitive to errors in the extinction calculation.

In particular, the disparity in angular resolution between the WFPC2 instrument used to observe the $H\beta$ line and the NICMOS camera used to observe the $Pa\alpha$ line (as much as a factor of four) artificially reduces the perceived $Pa\alpha$ surface brightness of features that are bright in $H\beta$ and $Pa\alpha$ but smaller than the NICMOS pixel size. This causes an artificially low value of A_V to be applied to the compact $H\beta$ region, and the $H\beta$/SFR to be underestimated. Careful inspection of the $H\beta$ images indicates that only several pixels in the PG 1448+273 and PG 2214+139 images are affected.

To determine the uncertainties in SFRs, we consider how points in the diagnostic diagrams of Fig. 6 would move around as a result of uncertainties in photometry, the value of A_V, and the choice of extinction law (see discussion in Sections 7 and 8.2). Thus, we apply appropriate shifts to these points in different directions and compute the SFR each time from the points that fall within the locus of H II regions. In each case, we also re-compute the SFR after excluding the points that fall in the overlap region between the H II region locus and the AGN narrow-line region locus of the diagnostic diagrams (see discussion in Section 8.2). As a result of

Table 7. Line luminosities after PSF subtraction, star-formation rates, and stellar masses.

	L(line)(10^{40} erg s^{-1})				SFR (M$_\odot$ yr^{-1})				log ($M_\star$/M$_\odot$)	
	[O II]	Hβ	[O III]	Paα	Hβ,Paα^a	[O II]^b	[Ne II]^c	FIR^d	K-band^e	H-band^f
PG 0026+129	220 ± 10	138 ± 4	260 ± 10	56.1 ± 0.5	16^{+6}_{-8}	6^{+1}_{-3}	13	<23	11.2	10.9
PG 0838+770	160 ± 50	70 ± 7	40 ± 3	21.0 ± 0.3	13^{+4}_{-7}	7^{+1}_{-5}	19	38	10.7	11.1
PG 1244+026	15 ± 1	7.3 ± 0.4	6.2 ± 0.3	2.95 ± 0.02	$2.0^{+0.5}_{-0.6}$	$1.0^{+0.2}_{-0.9}$	6	11	10.2	–
PG 1307+085	460 ± 70	130 ± 10	63 ± 4	57.0 ± 0.6	28^{+9}_{-11}	14^{+2}_{-9}	26	44	11.2	10.8
PG 1448+273	200 ± 20	130 ± 8	102 ± 3	19.7 ± 0.1	16^{+6}_{-12}	11^{+1}_{-7}	6	–	11.0	–
PG 1613+658	770 ± 80	220 ± 10	220 ± 20	91.1 ± 0.8	53^{+19}_{-25}	25^{+8}_{-22}	171	114	11.3	11.5
PG 1626+554	127 ± 3	119 ± 2	50 ± 2	–	19^{+3}_{-14}	10^{+2}_{-2}	3	21	–	10.8
PG 2214+139	300 ± 90	97 ± 7	85 ± 7	31.6 ± 0.2	23^{+5}_{-12}	7^{+1}_{-3}	3	11	11.1	11.0

^{a}Derived from an average of Hβ and Paα luminosities, as described in Section 8.4. The uncertainties include photometric errors as well as all uncertainties associated with extinction corrections (see Sections 7, 8.2 and 8.4).
^{b}Derived from the [O II] luminosities, as described in Section 8.4. The range of values reflects the uncertainties discussed in Sections 7, 8.2 and 8.4.
^{c}Derived from the [Ne II] 12.8 μm luminosities from (Schweitzer et al. 2006, see our Table 1), using the prescription of Ho & Keto (2007).
^{d}Derived from the FIR luminosity listed in Table 1 as described in Section 8.4.
^{e}Stellar masses derived from galaxy-only K-band continuum luminosities from this work, as described in Section 9.3. The uncertainty is ±0.2 dex.
^{f}Stellar masses derived from galaxy-only H-band continuum luminosities reported by Veilleux et al. (2009), as described in Section 9.3. The uncertainty is ±0.3 dex.

the last issue, the lower error bar is often larger than the upper error bar. We report the resulting SFRs and their error bars in Table 7.

To verify the above results, we compare the SFRs obtained from the hydrogen lines to other star-formation indicators. In Table 7, we list SFRs computed from the [O II] luminosities and the prescription from equations 10 and 11 of Kewley, Geller & Jansen (2004), which take into account the metallicity of the gas (we obtain error bars by the method described above). The metallicities we employ are derived from equation 11 of Kewley et al. (2004) and turn out to be close to the solar value. The [O II] SFRs we obtain, listed in Table 5, are, on average, a factor of 2 lower than those obtained from the hydrogen lines. If instead we used metallicities that are twice the solar value (see, for example, Storchi-Bergmann et al. 1998), the [O II] SFRs would be in good agreement with the hydrogen line SFRs.[5] Given the uncertainty in metallicity, we prefer the SFRs derived from the hydrogen lines. For comparison, we also list in Table 7 SFRs based on two other indicators: (a) the FIR luminosities from Table 1 (the prescription of section 2.5 of Kennicutt 1998) and (b) the luminosity of the [Ne II] 12.8 μm line from Table 1 (following the prescription of Ho & Keto 2007). The SFRs derived from the FIR luminosity are on a par with or somewhat higher (by a factor of approximately 2) than those obtained from our measurements, which may be a result of contamination by FIR emission from the quasar central engine. The SFRs derived from the [Ne II] luminosity are on a par with or somewhat lower than those obtained from our measurements. These two indicators yield a higher dispersion in SFRs but they still give approximately the same range in SFRs as our measurements, specifically, PG 1626+554 consistently has the highest SFR by all indicators, PG 1244+026 appears to have

the lowest SFR, and all other objects have SFRs of a few tens of M$_\odot$ yr^{-1}.

8.5 Line-emitting region sizes

The spatially resolved host galaxy images enable this study to test the AGN narrow-line region size versus luminosity relation reported by Bennert et al. (2002); this is based on the assumption that the extended line-emitting regions are, in fact, AGN narrow-line regions. The reported relation spans almost three orders of magnitude in luminosity and includes Seyfert galaxies and nearby quasars. However, Netzer et al. (2004) fail to find extended [O III] emission in their set of high-luminosity quasars, and argue that the extended emission-line luminosity reported in Bennert et al. (2002) is most likely powered by star formation at large distances from the quasar on the grounds that extrapolating this relationship to large quasar luminosities yields AGN narrow-line regions larger than many galaxies, and much larger than any observed. Here, we describe the procedure used to determine the size of the line-emitting region in each host galaxy and we use our results in Section 9.2 to evaluate the report by Bennert et al. (2002).

We report the 90 per cent and 95 per cent light radii in Tables 8 and 9, respectively. The values were determined by taking successively

---

[5] All the star-formation indicators used here adopt the Salpeter stellar IMF for the calibration. Kewley et al. (2004) assume an upper limit of 120 M$_\odot$ for the IMF while all other indicators are calibrated assuming an upper limit of 100 M$_\odot$ (Kennicutt 1998). This difference contributes somewhat to the lower SFRs obtained from the luminosity of the [O II] luminosities.

Table 8. 90 per cent light radii (kpc).

Object	Optical Cont.	[O II]	Hβ	[O III]	Paα	IR Cont.
PG 0026+129	1.60	4.43	3.72	4.43	0.88	4.35
PG 0838+770	0.46	4.62	0.59	4.62	0.90	3.65
PG 1244+026	1.24	0.28	0.55	0.28	1.04	0.53
PG 1307+085	5.07	1.38	3.26	1.38	0.98	5.04
PG 1448+273	0.37	0.34	1.79	0.34	1.27	0.54
PG 1613+658	2.91	1.16	5.36	1.16	1.45	1.23
PG 1626+554	1.14	0.62	0.60	0.62	–	–
PG 2214+139	1.45	2.76	1.51	2.76	1.21	0.94

Table 9. 95 per cent light radii (kpc).

Object	Optical Cont.	[O II]	Hβ	[O III]	Paα	IR Cont.
PG 0026+129	1.61	4.48	3.77	4.48	1.04	4.39
PG 0838+770	0.53	4.67	5.25	4.67	1.16	3.68
PG 1244+026	1.25	2.70	0.69	2.70	1.23	0.62
PG 1307+085	5.13	1.83	3.29	1.83	1.20	5.09
PG 1448+273	0.57	0.44	1.81	0.44	1.65	0.93
PG 1613+658	2.93	1.65	5.42	1.65	1.80	1.52
PG 1626+554	1.48	0.82	6.33	0.82	–	–
PG 2214+139	1.47	2.79	1.52	2.79	1.53	1.13

larger apertures around the quasar host galaxies and finding the asymptotic (i.e. total) emission-line flux, and then repeating the exercise to find the aperture size that encloses 90 per cent and 95 per cent of the total flux. The sizes we measure range from several tenths to several kpc, and are generally very similar for 90 per cent and 95 per cent light radii, indicating that these estimates of size are convergent and represent reasonable metrics for the size of the line-emitting region within each quasar host galaxy. In each of the emission-line images, we see the extended line-emitting regions centred on the location of the quasar.

9 DISCUSSION

9.1 Host galaxies

We measure at least some galaxy light in each filter for each quasar. The host galaxies are typically brighter and more easily seen in the infrared images, and faintest in the optical continuum images. With a few exceptions, we see little evidence of structure other than smooth, azimuthally symmetric light profiles. The charge transfer inefficiency streak is visible in many of the WFPC2 images, even after removal of the quasar PSF. Near the centre of the majority of the images there is noise from the PSF subtraction, visible as mottled dark and light pixels. Even with a correctly aligned PSF and a correctly computed PSF scalefactor, counting noise in the PSF image as well as minute variations in the telescope optics still unavoidably cause some differences between the quasar and model PSF, resulting in imperfect subtraction in some pixels.

Through the process of computing and removing the continuum from the optical narrow-band images, we find that the continuum is not a significant contribution. We expected relative faintness of the galaxies in the optical continuum because the galaxy flux density is much higher in the emission lines. The flux density of the infrared continuum is much higher compared to the Paα emission line than the optical continuum is compared to the optical emission lines, making it a larger though still a small contribution to the Paα emission-line flux.

The morphological character of the galaxies is typically unaffected by extinction correction. Even though the computed whole-galaxy line luminosities are larger after extinction correction, the S/N is lower due to the large uncertainty in the extinction correction (as described in Section 7). The background noise in the images takes on a cobbled appearance, partly due to the larger NICMOS pixels in the Paα images, and partly due to the need to bin and average the line-ratio maps (as described in Section 6.2).

With visual inspection, we can confidently attribute late-type morphology to only PG 0838+770, which is an edge-on disc whose

late-type morphology was not specifically known until these observations. The disc structure of PG 0838+770 is clearly visible in the Paα and the infrared continuum image, and the Paα brightness indicates star-forming activity along the disc as well as in the nucleus. The remaining host galaxies we have observed do not exhibit clear spiral or disc morphology. To visual inspection, they are broadly consistent either with early-type galaxies or the bulges of late-type galaxies. We see patchy extinction and line emission in some objects; for instance, the A_V maps for PG 1448+273 and PG 2214+139 in Fig. 5 show localized patchy clumps of higher extinction less than a kpc in size scattered around the core. PG 1448+273 has an extremely compact region of Hβ emission approximately 0.2 from its centre. This Hβ knot coincides with a region of relatively high extinction ($A_V \approx 2$ in Fig. 5) with line ratios that indicate star-formation (see Fig. 6). Interestingly, it is also embedded in a larger plume in the [O III] image.

Additionally, a galaxy near PG 1613+658 reported by Yee & Green (1987) is easily visible in the infrared continuum image and the Paα image prior to continuum removal. Without redshift information neither we nor Yee & Green (1987) can confirm an association between these objects. The separation is quite close (1 arcsec) and the angular size is comparable (0.5 versus 0.8), suggesting that the two galaxies are indeed related. Additionally, Yee & Green (1987) report that PG 1613+658 is coincident with a poor cluster of galaxies at the same redshift, providing a pool of potential interaction partners, and that there is a tidal tail to the east of PG 1613+658, suggesting recent interaction. However, after removing the continuum contribution to the Paα images (see Section 6.1), the companion nearly disappears. This suggests that either it is intrinsically Paα faint, or it is at a different redshift.

9.2 The extended line-emitting regions

As described in Section 8.2, we use emission-line diagnostics, shown in Fig. 6, to determine whether the line emission is powered by AGN photoionization or star formation at each point in the host galaxy. The observed line ratios imply that most of the emission-line flux from the extended line-emitting regions is powered by star formation. Moreover, only a few small sections, less than a few hundred pc in size, near the nuclei of several of the objects have [O III]/Hβ ratios greater than 10, which is an unambiguous signature of AGN narrow-line regions. In particular, we see high [O III]/Hβ ratios near the nucleus of PG 0026+129, our most luminous quasar (see below for further discussion). Based on these results and the estimates presented in Section 8.3, the AGN narrow-line region is very compact and is unresolved by our images.

This finding, that the majority of the line emission is from star-forming regions and that the AGN narrow-line regions are less than a few hundred pc in size, favours the interpretation of quasar host galaxy line emission discussed in Netzer et al. (2004), and suggests that the narrow-line region size to luminosity relation put forth in Bennert et al. (2002) does not extend into the high-luminosity regime of quasars. We do see sizes and luminosities consistent with the relations reported in Bennert et al. (2002), plotted in Fig. 8, but we conclude that only small portions of these line-emitting regions are AGN narrow-line regions. Azimuthally averaged line ratios (Fig. 7), which have a much higher S/N than the line-ratio diagnostic diagrams and maps in Fig. 6, also indicate [O III]/Hβ ratios which are too low for AGN narrow-line regions but consistent with star formation. The exception is near the very centres of several objects, where the line ratios are consistent with AGN narrow-line regions.
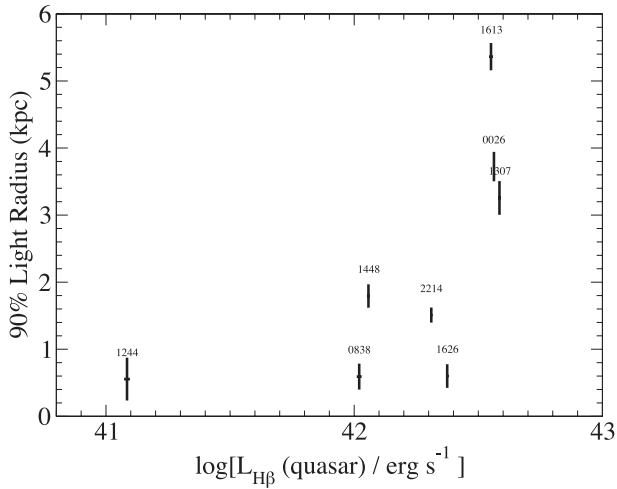
Figure 8. Radius containing 90 per cent of the Hβ light plotted against the quasar Hβ luminosity, following Bennert et al. (2002). The quasar Hβ luminosities used here represent the portion of the Hβ light removed from the Hβ images by the PSF subtraction process. Thus, these Hβ luminosities include the sum of the broad Hβ luminosity and the luminosity of the underlying continuum, with a very small contribution from narrow Hβ (see Section 8.1 for details).

9.3 Star-formation rates and their implications

We list the host galaxy emission-line luminosities along with the implied SFRs, determined as described in Section 8.4, in Table 7. We find typical rates of a few to several tens of $M_\odot$ yr^{-1}, but ranging from 2 to 65 $M_\odot$ yr^{-1}.

Our results are not in agreement with the results of Ho (2005), who infers low SFRs (typically around a few $M_\odot$ yr^{-1}). In particular, Ho (2005) reports SFRs of 6.0 and 0.57 $M_\odot$ yr^{-1} for PG 1613+658 and PG 2214+139, respectively, while we find values an order of magnitude or more higher. The disagreement between our [O II] SFRs and those of Ho (2005) is primarily a result of different extinction corrections. Ho (2005) assumes $A_V = 1$ for all the objects in his sample, whereas we determine A_V from our measurements. We obtain an average value of $A_V = 1.9$, which leads to a correction that is three times higher than that applied by Ho (2005). Moreover, in a substantial fraction of our objects we obtain higher values of A_V than the average. Another factor potentially contributing to the disagreement is the assumption made by Ho (2005) than only 1/3 of the observed [O II] luminosity should be attributed to star formation. Since we find that a substantial fraction of the [O III]λ5007 luminosity originates in the extended, star-forming regions around the nucleus, a higher fraction of the [O II] luminosity can also be attributed to star formation.

We plot the measured SFRs against quasar (blue) continuum luminosity in Fig. 9, where we see a clear trend of increasing SFR with increasing quasar luminosity. This re-affirms findings by other authors that black hole growth is closely tied to star formation in the host galaxy and growth of its stellar mass (e.g. Netzer et al. 2007; Netzer 2009; Mullaney et al. 2012; Rosario et al. 2013, and references therein). We illustrate our results further in Fig. 10, where we plot SFR against host galaxy stellar mass. The stellar masses are determined from our galaxy-only NICMOS continuum luminosities using established mass-to-light ratios (Bell et al. 2003), and are listed in Table 7. To verify the stellar masses obtained above, we have also used the *H*-band magnitudes of the host galaxies of six of the eight quasars in our sample (from Veilleux et al. 2009) to
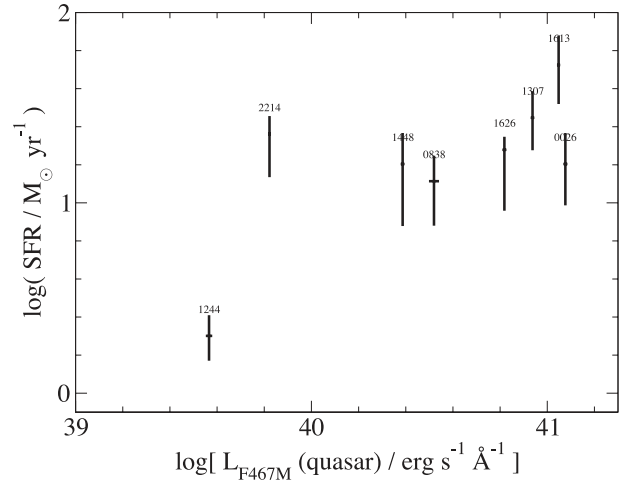

Figure 9. SFRs plotted against quasar continuum luminosity density in the *F467M* filter. This luminosity represents the portion of the light removed from the optical continuum images by the PSF subtraction.
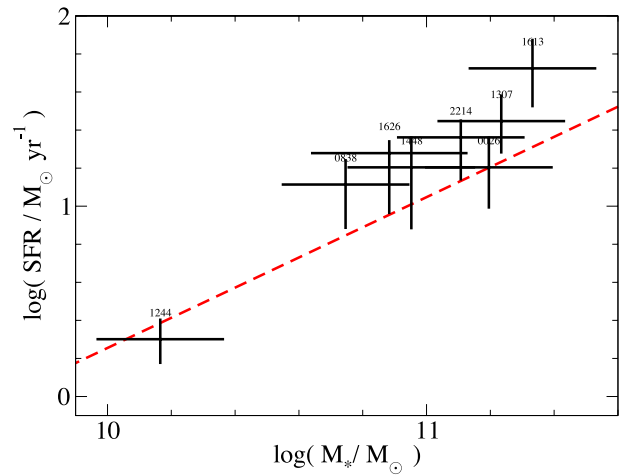
Figure 10. SFRs plotted against galaxy stellar mass, obtained by rescaling the infrared continuum luminosities as described in Section 9. The diagonal dashed line (red) shows the star-formation mass sequence derived by Whitaker et al. (2012), evaluated at the redshift of our sample.

compute the stellar masses, using the method of Bell & de Jong (2001)[6], and we list those results in Table 7 as well. The values from the two different methods agree to a factor of 2.5 or better. We see a trend of increasing SFR with increasing stellar mass, which reinforces the paradigm of galaxy growth tied to black hole growth. We also plot in this figure the star-formation mass sequence (or main sequence of star-forming galaxies; see, for example, Elbaz et al. 2007) using the equations of Whitaker et al. (2012) for the redshift of our targets. Our targets lie systematically above this relation in the region occupied by AGNs and/or starbursts, according to Whitaker et al. (2012).

---

[6] For the host galaxies in our sample we have used $B - V = 0.75$, assuming that they are similar to the nearby galaxies in the catalogue of Gil de Paz et al. (2007, 2009). The *H*-band mass-to-light ratio is more sensitive to the $B - V$ colour of the host galaxy than the *K*-band mass-to-light ratio. Therefore, we prefer the masses derived from the *K*-band luminosity. Moreover, the samples that we compare with in later sections of this paper have galaxy masses derived from the *K*-band luminosity.
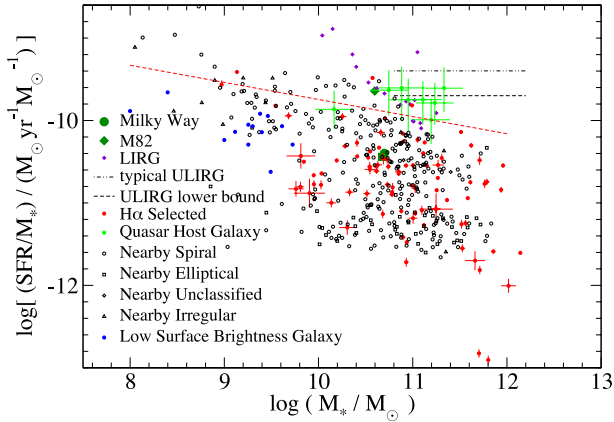
Figure 11. Mass specific SFR versus stellar mass for the quasar host galaxies reported in this work, along with several comparison samples: nearby galaxies (including M31) (Gil de Paz et al. 2007, 2009), Hα-selected galaxies (Young et al., in preparation), low surface brightness galaxies (Kuzio de Naray & Spekkens 2011), LIRGs (Lehmer et al. 2010), the Milky Way (McKee & Williams 1997; Hammer et al. 2007) and M82 (Heckman et al. 1990). The horizontal dot–dot–dashed line in the upper right quadrant of the plot marks the typical value of the specific SFR of ULIRGs, while horizontal dashed line just below it marks the lower bound on the specific SFR of ULIRGs. The diagonal dashed line (red) shows the star-formation mass sequence derived by Whitaker et al. (2012), evaluated at the redshift of our sample. Note that both the quasar host galaxies and the LIRGs fall on the upper envelope of normal star-forming galaxies, i.e. above the star-formation mass sequence; see Section 9.3.

To put these SFRs in the broader context of galaxy evolution, we plot in Fig. 11 specific SFR (SFR per unit stellar mass) against stellar mass for each of the seven of our quasar host galaxies for which we have NICMOS imaging, as well as for nearby galaxies (Gil de Paz et al. 2007, 2009), Hα selected galaxies (Young et al., in preparation), low surface brightness galaxies (Kuzio de Naray & Spekkens 2011), LIRGs (Lehmer et al. 2010), the Milky Way (McKee & Williams 1997; Hammer et al. 2007), M82 (Heckman, Armus & Miley 1990) and typical ULIRGs (Feruglio et al. 2010). In the same figure, we also indicate the star-formation mass sequence, as we did in Fig. 10.

The quasar host galaxies from our sample plotted in this figure have specific SFRs on a par with that of the starburst galaxy M82 and comparable to those of many Luminous Infrared Galaxies (LIRGs). However, their specific SFRs are not as high as those of ULIRGs of the same stellar mass (e.g. Sanders 2001; Veilleux et al. 2006). Their location just above the star-formation mass sequence suggests that they are in a starburst mode (see discussion in Elbaz et al. 2011). The exception is PG 1244+026, whose mass-specific SFR is well within the locus of normal galaxies. Not surprisingly, this object also has the least luminous quasar and the lowest SFR. While the quasar host galaxies in our sample have higher SFRs than typical star-forming galaxies, their rates are at the low end of theoretical predictions for peak SFRs for quasar-host galaxies. This may be a consequence of the galaxies being past their star-formation peaks, which would be consistent with a delay between the peak of star formation and the peak of black hole accretion as suggested by other observations that find star-formation episodes that ended a few hundred Myr ago in local, moderately to very luminous active galaxies (e.g. Davies et al. 2007; Schawinski et al. 2009; Wild, Heckman & Charlot 2010). However, a substantially larger sample of objects and spectroscopic data accompanied by a more sophisticated analysis (such as that of Cales et al. 2013) are needed to verify this picture.
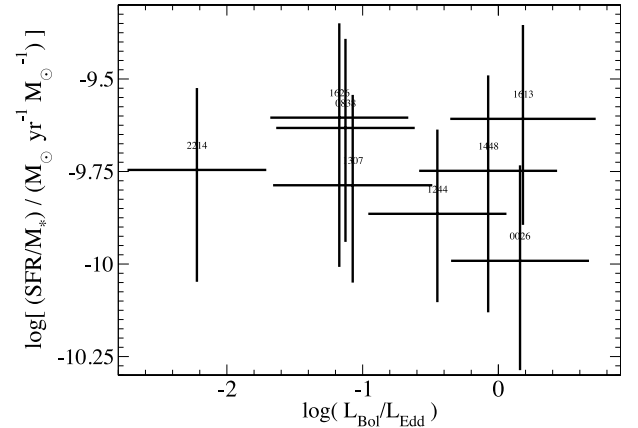
Figure 12. Mass specific SFR versus quasar Eddington ratio. The Eddington ratios were derived from the black hole masses in Table 1 and the quasar optical continuum luminosities. The galaxy stellar masses were obtained by rescaling the infrared continuum luminosities as described in Section 9.3.

Finally, in Fig. 12 we plot SFR per galaxy stellar mass versus the Eddington Ratio for the central black holes. To compute the Eddington Luminosities, we utilized the central black hole masses listed in Table 1. To compute the bolometric luminosities, we used the optical continuum luminosity densities of the quasars which were derived from the fluxes of the scaled PSF in the *F*467*M* filter. By using these quasar-only images, we are assured that the bolometric luminosities are not contaminated with galaxy light. We converted the luminosity densities to bolometric luminosities using an average quasar SED (Richards et al. 2006), and applying the bolometric correction corresponding to the *B* filter (similar to the *F*467*M* filter). The fact that no trend is evident in this figure indicates that these quasar host galaxies are not simply scaled versions of each other; the black hole growth rate spans two orders of magnitude in a very narrow range of specific SFR. This may be the result of these object being in different relative phases in the quasar life-cycle.

10 SUMMARY AND CONCLUSIONS

The eight quasar host galaxies presented in this work have extended line-emitting regions with sizes ranging from 0.5 to 5 kpc. We conclude, based on a study of the emission-line ratios, that these are star-forming regions. We measure SFRs of a few tens to several tens of $M_\odot$ yr^{-1}, substantially higher than those determined by Ho (2005) from spectroscopic observations of the [O II] lines. We have traced the difference in our results to different extinction corrections. PG 1244+026 has the lowest SFR, around $2\,M_\odot$ yr^{-1}; this is a small galaxy, with a stellar mass around $10^{10}\,M_\odot$. There is a strong trend between SFR and quasar luminosity, and also between SFR and galaxy stellar mass, reinforcing the paradigm that stellar populations and central black holes grow together. The host galaxies of our target quasars are located above the star-formation mass sequence in the specific star formation versus stellar mass diagram, which suggests a similarity with (U)LIRGs. However, we do not find any trend between the specific SFR and the black hole Eddington ratio, which indicates that the quasars are not just scaled versions of each other; this may be an indication that our target quasars are at varying stages in their life cycles. Finally, we note that, in view our results that the extended line-emitting regions in the quasar host galaxies are, in fact, dominated star-forming regions, any correlation between quasar luminosity and AGN narrow-line region size proposed should be considerably flatter than what was proposed by

Bennert et al. (2002). Indeed, later works find a flatter slope for this relation (Greene et al. 2011; Liu et al. 2013) and hint that it levels off at quasar luminosities (Hainline et al. 2013).

REFERENCES

Bahcall J. N., Kirhakos S., Saxe D. H., Schneider D. P., 1997, ApJ, 479, 642
Baldwin J. A., Phillips M. M., Terlevich R., 1981, PASP, 93, 5
Bell E. F., de Jong R. S., 2001, ApJ, 550, 212
Bell E. F., McIntosh D. H., Katz N., Weinberg M. D., 2003, ApJS, 149, 289
Bennert N., Falcke H., Schulz H., Wilson A. S., Wills B. J., 2002, ApJ, 574, L105
Bettoni D., Falomo R., Fasano G., Govoni F., 2003, A&A, 399, 869
Boroson T. A., Green R. F., 1992, ApJS, 80, 109
Bouchet P., Lequeux J., Maurice E., Prevot L., Prevot-Burnichon M. L., 1985, A&A, 149, 330
Boyce P. J. et al., 1996, ApJ, 473, 760
Boyce P. J. et al., 1998, MNRAS, 298, 121
Brocklehurst M., 1971, MNRAS, 153, 471
Cales S. L. et al., 2011, ApJ, 741, 106
Cales S. L. et al., 2013, ApJ, 762, 90
Calzetti D., Kinney A. L., Storchi-Bergmann T., 1994, ApJ, 429, 582
Calzetti D. et al., 2007, ApJ, 666, 870
Cardelli J. A., Clayton G. C., Mathis J. S., 1989, ApJ, 345, 245
Cid Fernandes R., Storchi-Bergmann T., Jr, Schmitt H. R., 1998, MNRAS, 297, 579
Cisternas M. et al., 2011, ApJ, 726, 57
Colina L., Garcia Vargas M. L., Gonzalez Delgado R. M., Mas-Hesse J. M., Perez E., Alberdi A., Krabbe A., 1997, ApJ, 488, L71
Cox T. J., Jonsson P., Somerville R. S., Primack J. R., Dekel A., 2008, MNRAS, 384, 386
Dasyra K. M. et al., 2007, ApJ, 657, 102
Davies R. I., Müller Sánchez F., Genzel R., Tacconi L. J., Hicks E. K. S., Friedrich S., Sternberg A., 2007, ApJ, 671, 1388
de Vaucouleurs G., 1959, Handb. Phys., 53, 275
Debuhr J., Quataert E., Ma C.-P., 2011, MNRAS, 412, 1341
Di Matteo T., Springel V., Hernquist L., 2005, Nature, 433, 604
Disney M. J. et al., 1995, Nature, 376, 150
Dopita M. A. et al., 2006, ApJS, 167, 177
Elbaz D. et al., 2007, A&A, 468, 33
Elbaz D. et al., 2011, A&A, 533, A119
Elvis M. et al., 1994, ApJS, 95, 1
Ferrarese L., Merritt D., 2000, ApJ, 539, L9
Ferrarese L., Pogge R. W., Peterson B. M., Merritt D., Wandel A., Joseph C. L., 2001, ApJ, 555, L79
Feruglio C. et al., 2010, ApJ, 721, 607

Förster Schreiber N. M., Roussel H., Sauvage M., Charmandaris V., 2004, A&A, 419, 501
Fruchter A. S., Hook R. N., 2002, PASP, 114, 144
Gabor J. M. et al., 2009, ApJ, 691, 705
Gebhardt K. et al., 2000, ApJ, 539, L13
Genzel R. et al., 2008, ApJ, 687, 59
Gil de Paz A. et al., 2007, ApJS, 173, 185
Gil de Paz A. et al., 2009, VizieR Online Data Catalog, 217, 30185
González Delgado R. M., Heckman T., Leitherer C., 2001, ApJ, 546, 845
Governato F. et al., 2009, MNRAS, 398, 312
Greene J. E., Zakamska N. L., Ho L. C., Barth A. J., 2011, ApJ, 732, 9
Groves B. A., Dopita M. A., Sutherland R. S., 2004a, ApJS, 153, 9
Groves B. A., Dopita M. A., Sutherland R. S., 2004b, ApJS, 153, 75
Guyon O., Sanders D. B., Stockton A. N., 2006, New Astron. Rev., 50, 748
Haas M. et al., 2003, A&A, 402, 87
Hainline K. N., Hickox R. C., Greene J. E., Myers A. D., Zakamska N. L., 2013, ApJ, 774, 145
Hamann F., Ferland G., 1999, ARA&A, 37, 487
Hammer F., Puech M., Chemin L., Flores H., Lehnert M. D., 2007, ApJ, 662, 322
Heckman T. et al., 1995, ApJ, 452, 549
Heckman T. M., Armus L., Miley G. K., 1990, ApJS, 74, 833
Heckman T. M., Gonzalez-Delgado R., Leitherer C., Meurer G. R., Krolik J., Wilson A. S., Koratkar A., Kinney A., 1997, ApJ, 482, 114
Hibbard J. E., van Gorkom J. H., 1996, AJ, 111, 655
Ho L. C., 2005, ApJ, 629, 680
Ho L. C., Keto E., 2007, ApJ, 658, 314
Hopkins P. F., 2009, in Jogee S., Marinova I., Hao L., Blanc G. A., eds, ASP Conf. Ser. Vol. 419, Galaxy Evolution: Emerging Insights and Future Challenges, Astron. Soc. Pac., San Francisco, p. 228
Hopkins P. F., Hernquist L., Cox T. J., Di Matteo T., Martini P., Robertson B., Springel V., 2005, ApJ, 630, 705
Hopkins P. F., Hernquist L., Cox T. J., Di Matteo T., Robertson B., Springel V., 2006, ApJS, 163, 1
Kaspi S., Smith P. S., Netzer H., Maoz D., Jannuzi B. T., Giveon U., 2000, ApJ, 533, 631
Kauffmann G., Haehnelt M., 2000, MNRAS, 311, 576
Kennicutt R. C., Jr, 1998, ARA&A, 36, 189
Kewley L. J., Dopita M. A., Sutherland R. S., Heisler C. A., Trevena J., 2001, ApJ, 556, 121
Kewley L. J., Geller M. J., Jansen R. A., 2004, AJ, 127, 2002
Kewley L. J., Groves B., Kauffmann G., Heckman T., 2006, MNRAS, 372, 961
Koekemoer A. M., Fruchter A. S., Hook R. N., Hack W., 2003, in Arribas S., Koekemoer A., Whitmore B., eds, Proc. 2002 HST Calibration Workshop, Hubble after the Installation of the ACS and the NICMOS Cooling System. Space Telescope Science Institute, Baltimore, MD, p. 337
Koornneef J., Code A. D., 1981, ApJ, 247, 860
Kormendy J., Richstone D., 1995, ARA&A, 33, 581
Kormendy J., Sanders D. B., 1992, ApJ, 390, L53
Krist J., 1995, in Shaw R. A., Payne H. E., Hayes J. J. E., eds, ASP Conf. Ser. Vol. 77, Astronomical Data Analysis Software and Systems IV, Astron. Soc. Pac., San Francisco, p. 349
Kuzio de Naray R., Spekkens K., 2011, ApJ, 741, L29
Lauer T. R. et al., 2005, AJ, 129, 2138
Lehmer B. D., Alexander D. M., Bauer F. E., Brandt W. N., Goulding A. D., Jenkins L. P., Ptak A., Roberts T. P., 2010, ApJ, 724, 559
Liu G., Zakamska N. L., Greene J. E., Nesvadba N. P. H., Liu X., 2013, MNRAS, 430, 2327
Lutz D. et al., 2008, ApJ, 684, 853
Marconi A., Hunt L. K., 2003, ApJ, 589, L21
McKee C. F., Williams J. P., 1997, ApJ, 476, 144
McLeod K. K., McLeod B. A., 2001, ApJ, 546, 782
McLure R. J., Dunlop J. S., 2001, MNRAS, 327, 199
Mullaney J. R. et al., 2012, MNRAS, 419, 95
Nagao T., Murayama T., Taniguchi Y., 2001, ApJ, 546, 744
Nagao T., Murayama T., Shioya Y., Taniguchi Y., 2002, ApJ, 567, 73
Nelson C. H., 2000, ApJ, 544, L91

Netzer H., 2009, MNRAS, 399, 1907

Netzer H., Shemmer O., Maiolino R., Oliva E., Croom S., Corbett E., di Fabrizio L., 2004, ApJ, 614, 558

Netzer H. et al., 2007, ApJ, 666, 806

Onken C. A., Peterson B. M., Dietrich M., Robinson A., Salamanca I. M., 2003, ApJ, 585, 121

Osterbrock D. E., 1989, Astrophysics of Gaseous Nebulae and Active Galactic Nuclei. University Science Books, Mill Valley, CA

Page M. J. et al., 2012, Nature, 485, 213

Richards G. T. et al., 2006, ApJS, 166, 470

Rigopoulou D. et al., 2009, MNRAS, 400, 1199

Rosario D. J. et al., 2013, preprint (arXiv:e-prints)

Sanders D. B., 2001, preprint (arXiv:e-prints)

Santini P. et al., 2012, A&A, 540, A109

Schawinski K., Virani S., Simmons B., Urry C. M., Treister E., Kaviraj S., Kushkuley B., 2009, ApJ, 692, L19

Schombert J. M., Wallin J. F., Struck-Marcell C., 1990, AJ, 99, 497

Schweitzer M. et al., 2006, ApJ, 649, 79

Seaton M. J., 1979, MNRAS, 187, 73p

Shemmer O., Netzer H., Maiolino R., Oliva E., Croom S., Corbett E., di Fabrizio L., 2004, ApJ, 614, 547

Springel V., Di Matteo T., Hernquist L., 2005, MNRAS, 361, 776

Storchi-Bergmann T., Schmitt H. R., Calzetti D., Kinney A. L., 1998, AJ, 115, 909

Sturm E. et al., 2011, ApJ, 733, L16

Tacconi L. J., Genzel R., Lutz D., Rigopoulou D., Baker A. J., Iserlohe C., Tecza M., 2002, ApJ, 580, 73

Tremaine S. et al., 2002, ApJ, 574, 740

Veilleux S., Osterbrock D. E., 1987, ApJS, 63, 295

Veilleux S. et al., 2006, ApJ, 643, 707

Veilleux S. et al., 2009, ApJ, 701, 587

Vestergaard M., Peterson B. M., 2006, ApJ, 641, 689

Volonteri M., Haardt F., Madau P., 2003a, ApJ, 582, 559

Volonteri M., Madau P., Haardt F., 2003b, ApJ, 593, 661

Weinzirl T., Jogee S., Khochfar S., Burkert A., Kormendy J., 2009, ApJ, 696, 411

Whitaker K. E., Kriek M., van Dokkum P. G., Bezanson R., Brammer G., Franx M., Labbé I., 2012, ApJ, 745, 179

Whitmore B., Heyer I., 1997, Technical report, New Results on Charge Transfer Efficiency and Constraints on Flat-Field Accuracy. Space Telesc. Sci. Inst., Baltimore

Whitmore B., Heyer I., Casertano S., 1999, PASP, 111, 1559

Wild V., Heckman T., Charlot S., 2010, MNRAS, 405, 933

Yee H. K. C., Green R. F., 1987, AJ, 94, 618

This paper has been typeset from a TEX/LATEX file prepared by the author.